

# The Forward and Inverse Problems of Electrocardiography

## *Gaining a Better Qualitative and Quantitative Understanding of the Heart's Electrical Activity*

**Ramesh M. Gulrajani**  
Institute of Biomedical Engineering  
Université de Montréal

**E**lectrocardiography involves the interpretation of the potentials recorded at the body surface due to the electrical activity of the heart. The general objective of the so-called "forward" and "inverse" problems of electrocardiography is a better qualitative and quantitative understanding of the heart's electrical activity. To this end we use the concept of a pre-decided electrical representation of the heart's activity, or, in other words, an "equivalent source," in conjunction with a specified volume conductor that is usually taken to be similar to the subject's torso. The equivalent source could be, for instance, a single current dipole or even a distribution of current dipoles. The forward problem of electrocardiography then consists of calculating the potential distribution generated at the surface of the specified volume conductor due to the presence of the selected equivalent source inside the conductor. The inverse problem, on the other hand, starts with the measured body-surface-potential distribution and attempts to adjust the parameters of the equivalent source so as to result in potentials on the surface of the specified volume conductor that most closely match the measured distribution.

In contrast to the forward problem, which can be solved uniquely to within a constant for the potential, the inverse problem does not possess a mathematically unique solution. The primary cardiac sources cannot be uniquely determined as long as the active cardiac region containing these sources is inaccessible for potential measurements [1]. This is because the electric field that these sources generate outside any closed surface completely enclosing them may be duplicated by equivalent single-layer

(monopole) or double-layer (dipole) current sources on the closed surface itself. Many equivalent sources, and hence inverse solutions, are thus possible. However, once an equivalent source (and associated volume conductor) is selected, its parameters can usually be determined uniquely from the body-surface potentials.

This article summarizes the theoretical underpinnings of both the forward and inverse problems of electrocardiography. Space limitations prohibit describing all of the research work done in these areas, and the author apologizes in advance for any omissions on this account or due to oversight. Additional details may be found in the author's recent text from which most of this material is drawn [2].

### **The Forward Problem**

The forward problem of electrocardiography entails the calculation of the body-surface potentials, starting usually from either equivalent current dipoles that represent the heart's electrical activity or from known potentials on the heart's outer surface (the "epicardium"). One of two general approaches is used, namely surface methods or volume methods. In surface methods, the different torso regions are all assumed to be of isotropic conductivity, and only the interfaces between the different regions are discretized and represented in the numerical torso model. If an anisotropic region such as the anisotropic-conductivity skeletal muscle layer overlying the ribs is included in the torso model, it is first converted to an approximately equivalent isotropic region before performing the forward computations. These computations entail the solution of integral equations for the potential on the discretized surfaces of the torso

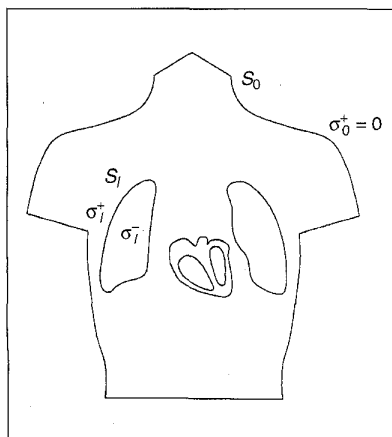
model. Surface methods are also termed boundary-element methods, since only the boundaries between torso regions enter into consideration. In volume methods, on the other hand, the entire three-dimensional torso model is represented numerically, usually by a combination of tetrahedral and hexahedral (brick-shaped) elements. Volume methods may be subdivided into finite-difference, finite-element, and finite-volume methods.

As may be expected, surface methods use simpler torso models with fewer elements. However, since the underlying integral equations couple the potential at every element to the potential at every other element, the coefficient matrix characterizing the set of equations to be solved is fully populated. Volume methods use more complex torso models, with more elements and consequently more potentials to be determined. However, the potential at each point is expressed only in terms of the potentials at its nearest neighbors. Consequently, the coefficient matrix, while large, is also sparse. Volume methods represent the only way to incorporate individual regions of *varying* conductivity.

### Surface Methods

#### Solutions from Equivalent Dipoles

As noted above, surface methods are based on integral equations for the potential derived by applying Green's second identity to the geometry of Fig. 1, which shows a torso containing multiple homogeneous regions of different isotropic conductivities. Here,  $S_0$  represents the



**1. Torso with multiple regions of differing isotropic conductivity. Note that the outer-torso surface,  $S_0$ , encloses all the other conductivity interfaces and that  $\sigma_0^+ = 0$ .**

## Volume methods represent the only way to incorporate individual regions of varying conductivity.

outer body surface, situated in air with conductivity zero, and  $S_l$ ,  $l=1,2,\dots,N_S$  closed internal interfaces separating homogeneous regions of isotropic conductivities:  $\sigma_l^-$  on the inside and  $\sigma_l^+$  on the outside. An application of Green's second identity then yields the following equation for the potential  $\Phi_k(\mathbf{r})$  on the surface  $S_k$  [3]:

$$\Phi_k(\mathbf{r}) = \frac{1}{2\pi(\sigma_k^- + \sigma_k^+)} \int \mathbf{J}_s(\mathbf{r}') \cdot \nabla' \left( \frac{1}{|\mathbf{r} - \mathbf{r}'|} \right) dV' + \frac{1}{2\pi} \sum_{l=0}^{N_S} \int_{S_l} \frac{(\sigma_l^- - \sigma_l^+)}{(\sigma_k^- + \sigma_k^+)} \Phi(\mathbf{r}') d\Omega_{rr'} \quad (1)$$

where  $\mathbf{J}_s$  ( $A/m^2$ ) denotes the density of the dipole heart sources,  $\mathbf{r}$  is the vector to the observation point, and  $\mathbf{r}'$  the variable position vector associated with the volume and surface integrations. Also,  $d\Omega_{rr'}$  is the solid angle subtended at the observation point,  $\mathbf{r}$ , by the surface element,  $dS'$ , associated with  $\mathbf{r}'$ . The term involving the "self solid angle" ( $d\Omega_{rr}$ ), representing the solid angle subtended at  $\mathbf{r}$  by the surface element containing  $\mathbf{r}$ , is excluded from the summation in Eq. (1), since the contribution of this self-solid angle, which equals  $2\pi$  if the surface in the vicinity of  $\mathbf{r}$  is smooth, is already incorporated as such in deriving Eq. (1). Note that the first term on the right side in Eq. (1) is proportional to the infinite-medium potential due to  $\mathbf{J}_s$ .

If we assume that the torso interfaces are discretized into  $N_T$  planar triangles and that the potential is constant over each triangle, then  $N_T$  equations such as Eq. (1) can be written as  $\mathbf{r}$  moves from triangle to triangle. These equations can

be represented by the following matrix equation:

$$\Phi = \mathbf{G} + \mathbf{A}\Phi \quad (2)$$

where  $\Phi$  is an  $N_T \times 1$  matrix of the desired triangle potentials,  $\mathbf{G}$  is an  $N_T \times 1$  matrix representation of the first terms on the right of the  $N_T$  equations, and  $\mathbf{A}$  is an  $N_T \times N_T$  matrix (with diagonal terms zero) that depends only on the torso geometry and conductivities. Equation (2) can be rewritten  $(\mathbf{I} - \mathbf{A})\Phi = \mathbf{G}$  where  $\mathbf{I}$  is an  $N_T \times N_T$  identity matrix. The coefficient matrix  $(\mathbf{I} - \mathbf{A})$  multiplying  $\Phi$  is singular on account of an eigenvalue  $\lambda = 1$  of  $\mathbf{A}$ . The singularity is a consequence of the fact that  $\Phi$  can only be determined up to a constant unless a zero reference for the potential is established. It is usually removed by "deflating" the matrix  $\mathbf{A}$ ; i.e., removing its offending eigenvalue and thereby converting  $\mathbf{A}$  to a deflated matrix,  $\mathbf{A}^*$ , so that we end up solving:

$$(\mathbf{I} - \mathbf{A}^*)\Phi^* = \mathbf{G} \quad (3)$$

It can be shown that the matrix  $\Phi^*$  in Eq. (3) contains the correct outer torso potentials; for internal surfaces,  $\Phi^*$  and  $\Phi$  differ by a constant. The deflation procedure in effect provides a potential reference by adjusting the sum of the potentials on the triangles of the outer torso surface to be zero. The set of nonsingular Eqs. (3) may be solved for  $\Phi^*$  either by iterative methods or, if the number of triangles is not too excessive, by direct inversion of the coefficient matrix  $(\mathbf{I} - \mathbf{A}^*)$  [4, 5].

#### Solutions from Epicardial Potentials

The calculation of the outer body-surface potentials from the epicardial-surface potentials was first described by Barr, et al. [6]. The torso model now comprises just these two surfaces, and the governing integral equation is again obtained by an application of Green's second identity to the assumed homogeneous region contained between these two surfaces. By allowing the observation point,  $\mathbf{r}$ , to first approach the body surface,  $S_B$ , and next the heart surface,  $S_H$ , we get the following two equations:

$$\Phi_B(\mathbf{r}) = -\frac{1}{4\pi} \int_{S_H} \frac{1}{r'_{BH}} \nabla' \Phi_H \cdot dS' + \frac{1}{4\pi} \int_{S_H} \Phi_H \nabla' \left( \frac{1}{r'_{BH}} \right) \cdot dS' - \frac{1}{4\pi} \int_{S_H} \Phi_B \nabla' \left( \frac{1}{r'_{BB}} \right) \cdot dS' \quad (4)$$

$$\begin{aligned}\Phi_H(\mathbf{r}) = & -\frac{1}{4\pi} \int_{S_H} \frac{1}{r_{HH}} \nabla' \Phi_H \cdot d\mathbf{S}' + \\ & \frac{1}{4\pi} \int_{S_H} \Phi_H \nabla' \left( \frac{1}{r_{HH}} \right) \cdot d\mathbf{S}' \\ & - \frac{1}{4\pi} \int_{S_B} \Phi_B \nabla' \left( \frac{1}{r_{HB}} \right) \cdot d\mathbf{S}'\end{aligned}\quad (5)$$

For clarity, we have explicitly identified epicardial and body potentials by the subscripts  $H$  and  $B$ , respectively. The scalar distance  $|\mathbf{r} - \mathbf{r}'|$  is now designated  $r'_{BH}$ , etc., with the first subscript denoting the location of  $\mathbf{r}$  and the second the location of  $\mathbf{r}'$ . The prime on  $r'_{BH}$ , etc., serves as a reminder that the variable of integration is  $\mathbf{r}'$ . Two sets of matrix equations may be obtained from Eqs. (4) and (5), respectively; the first as the observation point sweeps all body-surface triangles and the second as the observation point sweeps all epicardial-surface triangles. We have:

$$\mathbf{A}_{BB} \Phi_B + \mathbf{A}_{BH} \Phi_H + \mathbf{B}_{BH} \Gamma_H = \mathbf{0} \quad (6)$$

$$\mathbf{A}_{HB} \Phi_B + \mathbf{A}_{HH} \Phi_H + \mathbf{B}_{HH} \Gamma_H = \mathbf{0} \quad (7)$$

In Eqs. (6) and (7),  $\Phi_B$  and  $\Phi_H$  are column matrices of potentials,  $\Gamma_H$  is a column matrix of epicardial potential gradients, and the various  $\mathbf{A}$  and  $\mathbf{B}$  coefficient matrices are determined solely by integrations involving the geometry of the epicardial and body surfaces. The first subscript of  $\mathbf{A}$  (or  $\mathbf{B}$ ) identifies the surface on which the observation points are selected, and the second whether the integration is over the heart or body surface. Equation (7) is solved for the matrix of epicardial potential gradients,  $\Gamma_H$ , which when substituted into Eq. (6) yields:

$$\Phi_B = \mathbf{T}_{BH} \Phi_H \quad (8)$$

where  $\mathbf{T}_{BH} = [\mathbf{A}_{BB} - \mathbf{B}_{BH} (\mathbf{B}_{HH})^{-1} \mathbf{A}_{HB}]^{-1} [\mathbf{B}_{BH} (\mathbf{B}_{HH})^{-1} \mathbf{A}_{HH} - \mathbf{A}_{BH}]$ . The elements of matrix  $\mathbf{T}_{BH}$  are the "transfer coefficients" relating the potential at a particular epicardial-surface point to that at a particular body-surface point, and they depend solely on the geometry of the epicardial and body surfaces.

Barr, et al. [6], also pointed out that it was computationally advantageous to select as the unknowns not the potential on each triangle but rather the potential at each triangle vertex. This is because for most surfaces the number of triangle vertices is approximately half the number of triangles, thus diminishing the size of the coefficient matrix. Also, in the experimental situation, where potentials are

measured on the heart or torso surface with electrodes, it is the positions of these electrodes that is used to triangularize the surface in question. The vertex approach then has the advantage that surface coordinates and potentials are known at the same set of locations. This vertex approach is also often used when body-surface potentials are to be computed from equivalent dipoles. If we denote by  $S_e$  a small environment of  $\mathbf{r}$  around the observation vertex on surface,  $S_k$ , then Eq. (1) is modified to:

$$\begin{aligned}& [\sigma_k^- (4\pi - \Omega_{rS_e}) + \sigma_k^+ \Omega_{rS_e}] \Phi_k(\mathbf{r}) \\ & = \int_{S_e} \mathbf{J}_s(\mathbf{r}') \cdot \nabla' \left( \frac{1}{|\mathbf{r} - \mathbf{r}'|} \right) dV \\ & + \sum_{i=0}^{N_e} \int_{S_i} (\sigma_i^- - \sigma_i^+) \Phi(\mathbf{r}') d\Omega_{r'}. \quad (9)\end{aligned}$$

where  $\Omega_{rS_e}$  is the self-solid angle subtended by  $S_e$  at  $\mathbf{r}$  (assuming  $\mathbf{r}$  is just inside  $S_k$ ). While the summation on the right side has no self-solid angle term, such a term is introduced via  $\Omega_{rS_e}$  into the left side, and hence into the diagonal terms of the resultant coefficient matrix. Since  $\Omega_{rS_e}$  is difficult to compute for  $\mathbf{r}$  at a nonsmooth vertex, one approximation is to set each diagonal term to be equal to the negative sum of all other matrix terms in its row, thereby rendering the coefficient matrix singular, as required. Other approximations are discussed by Meijs, et al. [7], and by Heller [8].

## Volume Methods

### Finite-Difference Method

The finite-difference method represents the torso geometry by a three-dimensional grid of discrete points or nodes. Resistive elements selected to reflect the intervening torso resistance are placed between the nodes. Kirchhoff's current law is written for each node, resulting in a large set of equations relating the potential between adjacent nodes. In effect, this method represents a discrete approximation to the governing equation

$$\nabla \cdot (\sigma \nabla \Phi) = -I_{sv} \quad (10)$$

where  $I_{sv} = -\nabla \cdot \mathbf{J}_s$  denotes the cardiac sources expressed in  $A/m^3$ . The accuracy of the solution depends upon the fineness of the node spacing and the accuracy with which the intervening resistances can be estimated. The set of equations is usually solved by Gauss-Seidel iteration with successive over-relaxation. The main draw-

backs of the finite-difference method are the large storage requirements and the slow convergence, although the latter can be mitigated somewhat by parallel processing. On the other hand, this method can handle any kind of boundary condition as well as varying volume conductor anisotropies. A good illustration of the application of the finite-difference method to electrocardiographic problems is to be found in Walker and Kilpatrick [9].

### Finite-Element Method

Here, the torso geometry is approximated by a set of contiguous volume elements of simple geometrical shapes such as tetrahedra or hexahedra. The finite-element method also solves Eq. (10), which governs the quasi-static determination of electrocardiographic potentials, in conjunction with mixed boundary conditions of the form:

$$\Phi = \Phi_a \text{ on } S_{01} \quad (11a)$$

$$(\sigma \nabla \Phi) \cdot d\mathbf{S} = J_n dS \text{ on } S_{02} \quad (11b)$$

In Eqs. (11),  $\Phi_a$  is a known applied voltage,  $J_n$  an injected normal current density, and the union of the disjoint surfaces  $S_{01}$  and  $S_{02}$  equals  $S_0$ , the entire outer torso surface. A finite-element solution to Eqs. (10) and (11) may be obtained by the technique of weighted residuals [10].

Assume that the potential can be approximated by

$$\hat{\Phi}(x, y, z) = \sum_{i=1}^m \beta_i(x, y, z) \Phi_i \quad (12)$$

where  $\Phi_i$  are the desired  $m$  unknown potentials in the volume conductor, and  $\beta_i$  are appropriate interpolating polynomials. Each  $\beta_i$  is equal to unity at node  $i$ , and is zero at all other nodes. If we substitute Eq. (12) into Eq. (10), we expect that on account of the approximation  $\hat{\Phi}$ :

$$\nabla \cdot (\sigma \nabla \hat{\Phi}) + I_{sv} = \mathbf{R} \quad (13)$$

where  $\mathbf{R}$  is a residual. The method of weighted residuals attempts to reduce  $\mathbf{R}$  to zero, but in a "weak form" whereby the set of weighted integrals below is zero:

$$\begin{aligned}& \int_V [\nabla \cdot (\sigma \nabla \hat{\Phi}) + I_{sv}] W_i dV \\ & = \int_V \mathbf{R} W_i dV = 0, i = 1, 2, \dots, m\end{aligned}\quad (14)$$

In the well-known Galerkin formulation, the weights  $W_i$  are selected to be the same as the interpolation polynomials  $\beta_i$ , and we get:

$$\int_V \beta_i [\nabla \cdot (\sigma \nabla \hat{\Phi})] dV + \int_{V_H} \beta_i I_{sv} dV = 0$$

$$i = 1, 2, \dots, m \quad (15)$$

Note that the second integral in Eq. (15) need only be evaluated over the heart region,  $V_H$ . The first integral is integrated by parts to obtain:

$$\int_S \beta_i (\sigma \nabla \hat{\Phi}) \cdot dS - \int_V (\sigma \nabla \hat{\Phi}) \cdot \nabla \beta_i dV$$

$$= - \int_{V_H} \beta_i I_{sv} dV \quad i = 1, 2, \dots, m$$

Since the potential is known on  $S_{01}$ ,  $\beta_i$  are zero there and we have, using Eq. (11b):

$$\int_V (\sigma \nabla \hat{\Phi}) \cdot \nabla \beta_i dV = \int_{V_H} \beta_i I_{sv} dV$$

$$+ \int_{S_{02}} \beta_i J_n dS, \quad i = 1, 2, \dots, m \quad (16)$$

Equation (16) also holds for each individual *volume element*, with  $i$  now ranging only over the  $r$  nodes belonging to that element. The interpolating polynomials,  $\beta_i$ , are usually taken to be linear and selected so that the potential is continuous across element interfaces. For internal volume elements, the surface integrals in Eq. (16) will cancel for contiguous elements owing to the continuity of the normal component of the current. As a result, when all the single-element equations are assembled, they can be written in a global matrix form as:

$$\mathbf{A}\Phi = \mathbf{F} \quad (17)$$

where  $\mathbf{A}$  is now a sparse  $m \times m$  coefficient matrix,  $\Phi$  is an  $m \times 1$  matrix of the unknown potentials, and  $\mathbf{F}$  is an  $m \times 1$  matrix that includes source and noncancelling terms from the right side of Eq. (16). While the Neumann boundary condition of Eq. (11b) enters naturally into  $\mathbf{F}$  (see Eq. (16)), a Dirichlet condition such as that of Eq. (11a) has to be incorporated explicitly by adjusting Eq. (17). Thus, if the potential  $\Phi$  at node  $i$  is  $\Phi_a$ , then all matrix elements,  $a_{ij}$ , in row  $i$  are set equal to zero, except  $a_{ii}$ , which is set equal to unity; in addition  $f_i$  is set equal to  $\Phi_a$ . This also renders  $\mathbf{A}$  nonsingular. Solutions to Eq. (17) may be obtained by iterative techniques, although many finite-element packages employ direct solvers based on sparse matrix techniques.

Equation (16) is also applicable to the computation of body-surface potentials from epicardial potentials, in which case, since the heart region  $V_H$  is excluded, the first integral on the right side drops out.

## The most evident application of the forward problem is in simulation of the electrocardiogram with computer heart models.

Since no current leaves the torso under these circumstances, the surface integral over  $S_{02}$  also disappears. The Dirichlet boundary condition at the epicardial surface is introduced as described above.

### Finite-Volume Method

The finite-volume method was first applied to the bioelectric problem by Abboud, et al. [11]. Here, the governing equation is the integral form of Eq. (10),

$$\oint_S \sigma \nabla \Phi \cdot dS = - \int_V I_{sv} dV \quad (18)$$

which is approximated numerically for each volume element in the torso model. The gradient required in Eq. (18) is estimated from its integral definition:

$$\nabla \Phi = \frac{1}{V} \oint_S \Phi dS \quad (19)$$

The mechanics of implementing the finite-volume method are described in [12]. The finite-volume approach is similar to the finite-element method, but with no a priori assumption for the variation of  $\Phi$  within an element, in the interests of accuracy it is essential that a fine discretization be employed. The final result is a large set of equations for the potentials at the center of each volume element. However, the coefficient matrix is sparse and the equations can be solved iteratively by the successive over-relaxation method.

Surface and volume methods can be combined such that the former are used where the torso is isotropic and the latter where it is anisotropic. This combination

takes advantage of any computational savings afforded by surface methods, while at the same time allows the handling of anisotropies. Such a combination of the transfer coefficient approach (Eq. (8)) and the finite-element method has been described by Stanley and Pilkington [13]. Starting from the epicardial potentials, the transfer coefficient approach is employed to compute the potentials at the *inner* surface of the anisotropic-conductivity skeletal muscle layer present beneath the torso. The finite-element method is then used to convert the potentials at this inner skeletal muscle interface to the desired torso surface potentials. The methodology of a combination method employing higher-order interpolation capable of matching the potential gradients as well as the potential across elements has been described by Pullan [14].

### Applications of the Forward Problem

The most evident application of the forward problem is in simulation of the electrocardiogram (ECG) with computer heart models. A second important application has been to study the effects of torso inhomogeneities on the ECG. Finally, the forward-problem methodology has also been used for the reciprocal problem of obtaining the currents traversing the heart due to current sources applied at the body surface. Examples of all three of these applications are given briefly here.

### Computer Heart Models

A two-step approach is employed to simulate the ECG with computer heart models. In the first step, a suitable propagation algorithm is used to excite the heart model and calculate the activation times of all model points. These times determine the model's activation isochrones. Next, equivalent source representations (usually current dipoles) are associated with these isochrones and are used to calculate the ECG by one of the methods described above. Some of the earlier heart models are of the nonpropagation type and assume a fixed set of activation isochrones based on data obtained in the isolated human heart by Durrer, et al. [15]. A particularly good example of this is the model developed by Miller and Geselowitz [16], which used a set of 23 regional current dipoles derived from the Durrer isochrones.

Heart models with an intrinsic propagation algorithm are much more versatile than fixed-activation models, and no

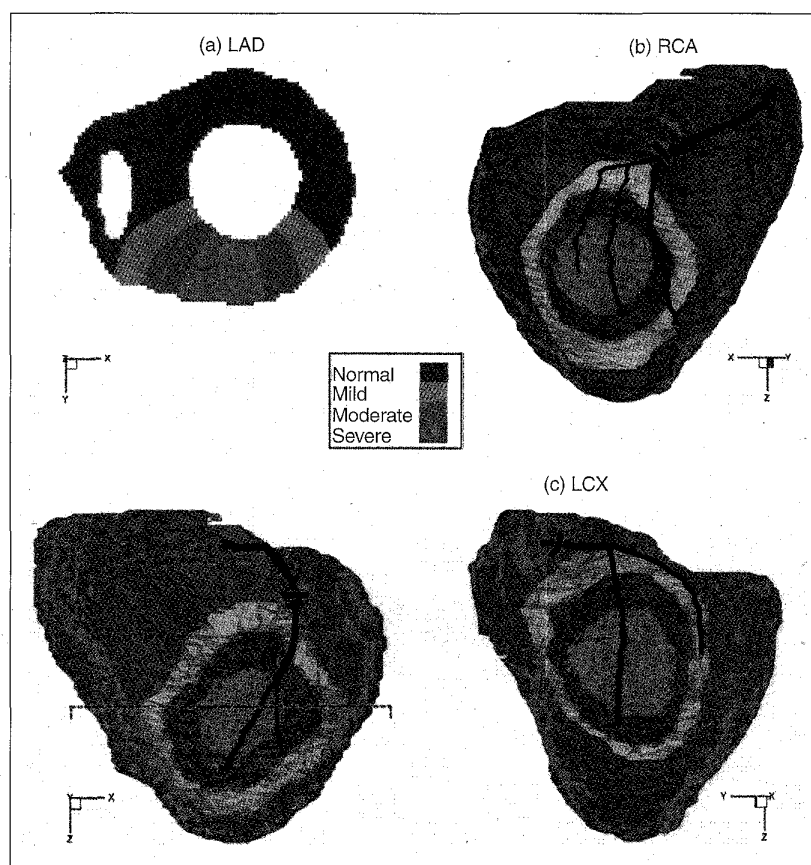
present-day model can afford not to include such an algorithm. In particular, the inclusion of propagation permits the simulation of cardiac pathologies occurring due to abnormalities of conduction. Propagation-type heart models originated with Okajima, et al. [17], and two of the better-known early ones are that of Solomon and Selvester [18, 19], and one developed at Dalhousie University in Halifax, Canada [20-22]. Since then, several groups around the world have developed propagation-type computer models of the heart, and by way of example only, we describe our own experience with such models.

Our heart-model anatomy was reconstructed as a three-dimensional array of 250,000 points, spaced 1 mm apart, based on data obtained from computed tomography scans of a human heart at autopsy [23]. The Purkinje conduction system in the heart was represented by a system of cables that fed onto a sheet of conduction tissue placed on the endocardium or inner surface of the heart. Approximately 1,120 "Purkinje-myocardium" junctions, present at the terminations of the cables as well as sprinkled uniformly over the sheet, transmitted the excitation from the conduction system to the ventricles. A stylized representation of myocardial fiber rotation was incorporated into the ventricles. The local fiber direction at each model point was used to compute the local propagation velocity of the activation front from the point in question to its nearest neighbors, assuming that the front could always be approximated as a plane wave. While myocardial anisotropy resulting from the fiber rotation was thus considered in the ventricular propagation process, it was, however, ignored in the computation of the equivalent dipole sources. These were computed by first associating a transmembrane action potential waveform with each model point, which was triggered upon activation of the point. The equivalent current dipole density,  $J_e$ , at each model point was then taken to be proportional to the spatial gradient of the transmembrane potential distribution. The elemental current dipoles at each point were summed vectorially within each of 88 heart-model regions. This 88-dipole heart model was positioned and oriented within an inhomogeneous torso model, and the body-surface potentials computed via Eq. (1). Initial work focused on simulating normal activation [23] and the major conduction

blocks [24]. The latter were simulated by blocking conduction at selected sites in the proximal cable portion of the specialized conduction system.

More recent work with our model involved simulating "ectopic" beats [25]. An ectopic beat is simply an abnormal cardiac beat, triggered at a site other than the sinoatrial node where excitation normally starts. Such a beat is easily simulated by starting model excitation at this alternative ectopic site. SippensGroenewegen, et al. [26], have suggested that the site of an endocardial ectopic beat can be determined from the surface potentials, and the model was used to verify their assertion. Our model was also used to simulate the effects on the ECG of regional

myocardial "ischemia" (i.e., reduced blood flow to a heart region) due to occlusion in either the left anterior descending (LAD), right coronary (RCA), or left circumflex (LCX) artery [27]. Model regions that correspond to the areas perfused by these arteries were demarcated and then further subdivided into three zones of mild, moderate, and severe ischemia, increasing progressively from the periphery of the ischemic region to the center (Fig. 2). The action-potential waveforms of each zone were modified to correspond to experimentally observed ischemic action potentials. These changes involve progressively reduced resting potential magnitudes, slower action-potential upstrokes, and diminished

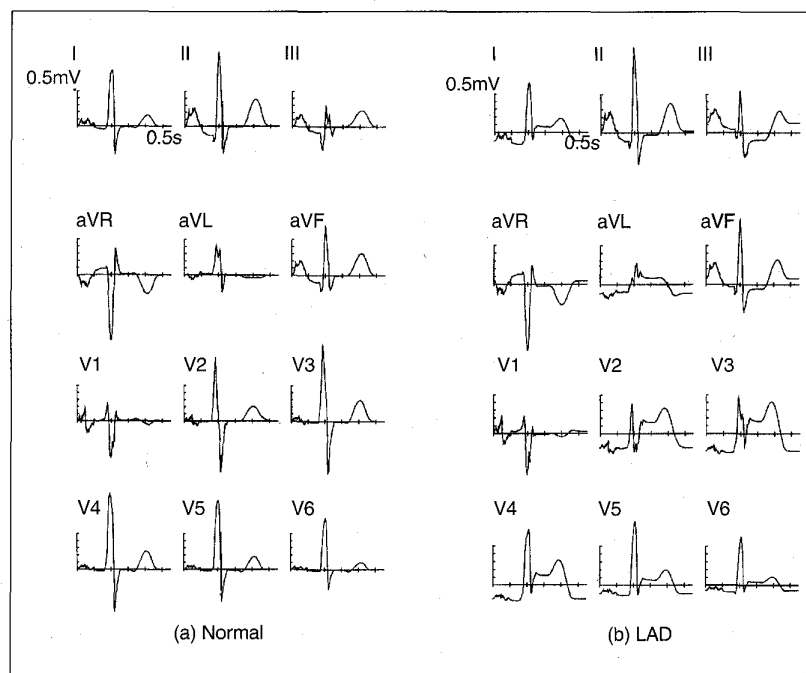


**2. Transverse and epicardial views of our model heart depicting the inserted ischemic regions. (a)** A transverse cross-section and an epicardial view are shown of the three assumed ischemic zones (mild, moderate, and severe) corresponding to occlusion of the left anterior descending artery (depicted schematically in red) at the site indicated by the black bar. The plane of the transverse cross-section is indicated by the dotted line in the epicardial view. **(b), (c):** Epicardial views are shown of the assumed ischemic zones, corresponding to occlusion at the black bar, of the right coronary and left circumflex arteries, respectively. Transverse cross-sectional views are not shown for these ischemic zones. The coordinate axes in (a), (b), and (c) depict the viewing angles used for each image (reproduced from [27], by permission of W.B. Saunders Co, Orlando, FL).

action-potential durations in the mild, moderate, and severely ischemic zones. While myocardial conduction velocities in the mildly ischemic zone were unaltered, those in the moderate and severely ischemic zones were reduced by 25% and 50%, respectively. For each of LAD, RCA and LCX occlusions, the heart model was re-excited with the above changes, and the ischemic ECG calculated. A comparison of the normal and of the ischemic ECG corresponding to LAD occlusion generated by the model is shown in Fig. 3.

#### Effects of Torso Inhomogeneities

The effects of torso inhomogeneities on the ECG have long been of interest to researchers. Early studies used physical torso analogs with artificial current-dipole sources to study the changes in potentials due to the insertion of materials of different conductivities, whose form mimicked the major torso inhomogeneities such as the intraventricular blood masses, lungs, and the skeletal muscle layer covering the rib cage. The more interesting early studies were, however, largely analytical, using spherical or cylindrical models of the heart and torso. Of these, the most significant was that of Brody [28], who elucidated what has come to be known as the "Brody-effect," whereby the high-conductivity blood in the ventricular cavities enhances body surface potentials due to dipoles oriented radial to these cavities and diminishes surface potentials due to dipoles oriented tangential to the cavities. This was demonstrated by assuming a spherical ventricular cavity filled with blood of infinite conductivity, which was placed in an infinite homogeneous medium representing ventricular myocardium in which the radial and/or tangential dipoles were situated. Another elegant series of simulations was done by Rudy and coworkers [29, 30] using an "eccentric-spheres" model in which the torso was represented by two systems of concentric spheres. The inner system, which mimicked the blood-filled cavity and myocardium, was eccentric with respect to the outer system, which represented the lungs, skeletal muscle, and subcutaneous fat. Besides verifying the Brody-effect for radial dipoles, Rudy and coworkers also described the effects of varying the conductivities of the lung, skeletal-muscle, and fat regions.



3. (a) Simulated ECGs for the normal heart. (b) Simulated ECGs for the heart with the ischemic region shown in Fig. 2(a) corresponding to occlusion of the left anterior descending artery (reproduced from [27], by permission of W.B. Saunders Co, Orlando, FL).

Numerical forward-problem methodologies have been particularly useful in investigating some of these inhomogeneity effects with realistic-geometry torso models. One such study, by Gulrajani and Mailloux [31], used a numerical torso model containing the skeletal muscle layer (introduced as an isotropic-conductivity region of enlarged thickness), the low-conductivity lungs, and two blood-filled high-conductivity intraventricular cavities. Since the inhomogeneities were represented by surfaces, Eq. (1) was used for potential computations. By introducing these inhomogeneities in cumulative fashion into an otherwise homogeneous torso (i.e., first the muscle layer, next the lungs, and finally the blood masses) and computing in each case the torso surface potentials due to the 23 individual current dipoles of the Miller-Geselowitz heart model, Gulrajani and Mailloux investigated the individual effects of these inhomogeneities on the dipole potentials. Furthermore, by using the specified normal activation sequence of the Miller-Geselowitz heart model, they also investigated the effects of these inhomogeneities on the normal ECG and the body-surface-potential map (BSPM). This last is a two-dimensional display of

the isopotential lines on an unrolled external torso surface. Most of Gulrajani and Mailloux's findings were in accordance with earlier work with realistic torso models [32-34]. At the level of the individual dipoles, the Brody-effect is operative for both radial and tangential dipoles. With regard to the normal ECG and BSPM, the major qualitative effects noted by Gulrajani and Mailloux were a smoothing of notches in the ECG and of isopotentials in the BSPM due to the blood masses, muscle layer, and, to a lesser extent, the lungs. There were also large quantitative effects on the ECG and BSPM, most notably magnitude increases due to the blood masses and magnitude decreases due to the muscle layer. The latter is due to the increased effective distance of the torso surface from the heart dipoles, and the former due to the Brody-effect acting on the predominantly radial orientation of the heart dipoles during normal excitation.

The advent of powerful computers has also seen an increased number of finite element and finite-difference models of the inhomogeneous torso being constructed as opposed to boundary-element models. One example is the finite-element model described by Johnson, et al. [35], which is based on magnetic resonance images of the torso. This model was used in a recent

three-dimensional finite-element study by Klepfer, et al. [36], of the effects of inhomogeneities and anisotropies on a known, fixed, epicardial potential distribution. Klepfer, et al., estimated 11 to 15% changes in the body-surface-potential distribution due to either addition or removal of one of the following inhomogeneities: lungs, anisotropic skeletal-muscle layer, or subcutaneous fat. They also found that inhomogeneities near the torso surface played a larger role than those near the heart. This finding, however, could be due to the fact that in their study, the starting epicardial potential distribution, being assumed as the source, was kept fixed and not "loaded" by the changing inhomogeneities. The intraventricular blood masses within the epicardium was not a factor in Klepfer, et al.'s, study. Another recent study [37] used a finite-difference reconstruction of the US National Library of Medicine's Visible Human Man data to study the effect of a 10% increase in conductivity of various organs on surface potentials due to a current dipole source placed in the heart region. The aim was to quantify the importance of uncertainties in the precise values of these conductivities on the surface potential. It was found that changing the conductivities of heart muscle, intracardiac blood masses, and anisotropic skeletal muscle had the most effect, whereas altering lung and subcutaneous fat conductivities had only a small influence.

#### Defibrillation

Often in a compromised heart the normal patterned excitation can degenerate into "ventricular fibrillation." In ventricular fibrillation, multiple chaotic wavelets are present in the ventricles, the pumping action of the heart is lost, and unless the heart is "defibrillated," death occurs in minutes. Defibrillation consists of applying a high-energy shock across the heart, with the idea being to simultaneously depolarize all the ventricular cells, thereby halting all fibrillatory activity. Upon recovery from the depolarizing shock, the sinoatrial node often recaptures control of the heart. Usually external or transthoracic defibrillation is used, whereby two large "paddle" electrodes are applied across the thorax and excited by a high-energy truncated exponential signal, obtained by discharging a capacitor across the electrodes and consequently through the thorax. For high-risk patients,

## The different solutions to the inverse problem may be presented according to the type of heart model whose parameters are being sought.

internal implantable defibrillators are now common, in which epicardial patches or intraventricular catheters serve as the defibrillating electrodes. These implantable defibrillators have circuitry to detect the onset of fibrillation, thereby automatically initiating the appropriate defibrillation protocols.

A certain minimum level of excitation is required at the heart for successful defibrillation, which translates to a minimum value of the applied current density everywhere in the heart. The number used in modeling studies is around 35 mA/cm<sup>2</sup> [38, 39]. At the same time, it is necessary that the current density anywhere in the heart does not exceed approximately 500 mA/cm<sup>2</sup>, since at these densities tissue damage is likely to occur. Therefore, it is important that the defibrillation electrodes used ensure a reasonably uniform current distribution throughout the heart.

The finite-element method represents the most direct approach to simulating defibrillation currents. For transthoracic defibrillation, Eq. (16) again forms the basis for deriving the finite-element matrix equation. In Eq. (16), the cardiac sources,  $I_{sv}$ , are set to zero for defibrillation simulations. Also, it is more correct to incorporate a Dirichlet boundary condition at the defibrillation electrodes, rather than suppose that these electrodes inject a uniform current density. Thus, there is no  $J_n$  in Eq. (16) either. Dirichlet boundary conditions at the epicardial patches or intraventricular catheter surfaces are also used when simulating internal defibrillation. Early studies just simulated the currents in an isolated heart [40], but in more recent work, the

heart is placed inside a torso model with Dirichlet conditions at the internal and/or external electrodes [41]. The torso models used in the above finite-element studies are necessarily complex, incorporating the different conductivities of the various internal organs and even representing the anisotropic conductivity of the skeletal muscle layer. Large sets of equations result, and Ng, et al. [42], discuss the use of massively parallel computers in solving these equations.

Transthoracic defibrillation simulations can also be run with the boundary-element formulation [43-46]. While the set of numerical equations is smaller, the disadvantage here is that anisotropic conductivity variations cannot be taken into account. The governing integral equation for the potential  $\Phi(\mathbf{r})$  anywhere in the volume conductor is again derived from an application of Green's second identity to the torso geometry of Fig. 1, and is [44]:

$$\begin{aligned}\Phi(\mathbf{r}) = & -\frac{1}{4\pi\sigma(\mathbf{r})} \sum_{i=0}^{N_s} \int_{S_i} (\sigma_i^- - \sigma_i^+) \\ \Phi(\mathbf{r}') \nabla' \left( \frac{1}{|\mathbf{r} - \mathbf{r}'|} \right) \cdot d\mathbf{S}' & \\ - \frac{1}{4\pi\sigma(\mathbf{r})} \int_{S_0} \frac{J_n(\mathbf{r}')}{|\mathbf{r} - \mathbf{r}'|} dS' & \quad (20)\end{aligned}$$

where  $\sigma(\mathbf{r})$  is the conductivity at the observation point and  $J_n(\mathbf{r}')$  is the normal component of the outward current density at the thoracic defibrillation electrodes. Oostendorp and van Oosterom [44] discuss the numerical solution of Eq. (20) for the unknown potentials and current densities in terms of the known potentials at the defibrillating electrodes.

Simulation studies on defibrillation have concentrated on determining the optimal positioning and size of the defibrillation electrodes in order to ensure an adequate and approximately uniform current density everywhere in the heart [39, 45-48]. One study focused on the sensitivity of the current-density distribution in the heart to variations in skeletal-muscle anisotropy [38]. It was found that in transthoracic defibrillation, whether the skeletal muscle was modeled as isotropic or anisotropic made little difference to current flow patterns in the heart, but simply affected current magnitudes. On the other hand, the same study showed that other inhomogeneities such as the lungs, ribs, and sternum affected both magnitudes and current patterns.



## The Inverse Problem

As already mentioned, the inverse problem does not possess a unique solution. This difficulty is circumvented by using simplified models for the cardiac current sources. These models introduce what van Oosterom and Huiskamp [49] have called "implicit" constraints that enable model parameters to be uniquely computed from the surface potentials. Examples of such models are a multipole series, one or two moving dipoles, multiple fixed-location dipoles, the epicardial potential distribution, and the activation isochrones on the heart surface.

A second characteristic of the inverse problem, not so easily bypassed, is its ill-posed nature, whereby the desired solution is unstable and can oscillate wildly with the slightest noise or perturbation in the electrical and/or geometrical input data. This ill-posed tendency increases with the number of parameters in the desired solution; i.e., with the complexity of the assumed heart model. The ill-posed nature needs to be stabilized, usually by the imposition of additional "explicit" spatial and temporal constraints on the parameters of the heart model.

The different solutions to the inverse problem may be presented according to the type of heart model whose parameters are being sought. Space limitations permit only an overview of solutions employing multipole coefficients, moving-dipole, or multiple-dipole models. Additional details of these models may be found elsewhere [50, 51]. Inverse solutions involving epicardial potentials or heart-surface isochrones are described more fully since they are the focus of considerable recent research [52].

### Inverse Solutions in Terms of Multipole Coefficients

In the multipole-series representation, the heart sources are characterized by an infinite series of multipolar current generators (dipole, quadrupole, octupole, hexadecapole, etc.), all located at a fixed common origin, usually chosen at the center of the heart. The series may be calculated by an approach suggested by Arthur, et al. [53]. Here, the subject's torso shape is modeled and, in an initial step, the transfer matrix,  $\mathbf{T}$ , relating unit multipole sources placed at an origin in the heart region to the surface potentials, is calculated via Eq. (3). This enables us to write:

$$\Phi = \mathbf{T}\mathbf{X} \quad (21)$$

where  $\Phi$  is an  $N \times 1$  matrix of surface potentials,  $\mathbf{X}$  is an  $M \times 1$  matrix of multipole coefficients, and  $\mathbf{T}$  is an  $N \times M$  transfer matrix. The important fact to note is that Eq. (21) is a *linear* matrix equation, characterized by the *constant* coefficients of  $\mathbf{T}$ . The constant coefficients arise specifically because the multipole origin is fixed, as also are the different electrode-site locations. Next, given a measured potential distribution characterized by the column matrix,  $\tilde{\Phi}$ , the multipole coefficient matrix,  $\mathbf{X}$ , is estimated from a standard linear least-squares minimization of the sum-squared residuals, given by:

$$\begin{aligned} \mathfrak{R} &= [\tilde{\Phi} - \Phi]^T [\tilde{\Phi} - \Phi] \\ &= [\tilde{\Phi} - \mathbf{T}\mathbf{X}]^T [\tilde{\Phi} - \mathbf{T}\mathbf{X}] \\ &= \|\tilde{\Phi} - \mathbf{T}\mathbf{X}\|^2 \end{aligned} \quad (22)$$

where  $\|\cdot\|$  denotes the Euclidean norm of a vector and the superscript  $T$  denotes the transpose. The solution is given by the so-called "normal equation" [54]:

$$\mathbf{X} = (\mathbf{T}^T \mathbf{T})^{-1} \mathbf{T}^T \tilde{\Phi} \quad (23)$$

In practice, if only the first few multipole coefficients are desired (up to and including octupole terms), Eq. (23) may be solved without too much difficulty. This solution is repeated for different values of  $\tilde{\Phi}$  during the cardiac cycle.

If a homogeneous torso model is assumed in determining  $\mathbf{T}$ , the multipole coefficients computed using measured surface potentials from a real *inhomogeneous* torso implicitly include the effects of the various inhomogeneities. If  $\mathbf{T}$  is computed using a torso model that includes the lungs, then the effects of the lungs will be separated out in the solution for  $\mathbf{X}$ . However, since residuals on the lung surfaces are not explicitly minimized, in order to guarantee convergence of the multipole series on these surfaces, they must fall outside a sphere circumscribed about the multipole origin that includes the cardiac sources. This condition precludes a similar compensation for the blood masses. Multipole solutions are sometimes used as an intermediate step in obtaining inverse solutions with more sophisticated inverse models (see below).

### Moving-Dipole Inverse Solutions

In these inverse solutions, the activity of the heart is represented by one or two moving current dipoles. The basic underlying principle is to select the amplitudes

and coordinates of these dipoles within an appropriate model of the torso such that the calculated torso-surface-potential distribution closely matches the measured body-surface-potential distribution. This selection is repeated for each time instant considered. Inverse solutions utilizing one or two moving dipoles are only justified when the real heart sources consist of one or two localized centers of activity, respectively. The hope then is that the coordinates of the calculated dipoles will indicate these sites of activity.

This solution also minimizes the squared residual of Eq. (22). For solutions in terms of moving dipoles, the matrix relation  $\Phi = \mathbf{T}\mathbf{X}$ , first expressed in Eq. (21), between the theoretically calculated surface potentials,  $\Phi$ , and the unknowns,  $\mathbf{X}$ , of the problem, is unfortunately no longer linear. The unknowns of the problem are now the three components *and* the three coordinates of the single-moving-dipole (SMD) model, with a corresponding doubling for the two-moving-dipole (TMD) model. The relation between the theoretical potential at an arbitrary site and the coordinates of the dipoles is profoundly nonlinear. Consequently, one can no longer use the normal Eq. (23) to effect a solution. Rather, nonlinear iterative techniques for minimizing the squared residual, such as the Levenberg-Marquardt algorithm [55], need to be employed.

If the forward transfer matrix,  $\mathbf{T}$ , relating dipoles to surface potentials may be obtained by direct matrix inversion of the coefficient matrix,  $(\mathbf{I} - \mathbf{A}^*)$ , in Eq. (3), the matrix of surface potentials can be rapidly computed at each iteration. Moreover, the Jacobian derivatives of the squared residual  $\mathfrak{R} = [\tilde{\Phi} - \Phi]^T [\tilde{\Phi} - \Phi]$  with respect to the  $X_j$  components of  $\mathbf{X}$ , also required by the Levenberg-Marquardt algorithm, can be determined from estimates of  $\partial\Phi/\partial X_j$ . With direct inversion, since  $\Phi^* = (\mathbf{I} - \mathbf{A}^*)^{-1} \mathbf{G}$ , we have [4]:

$$\frac{\partial\Phi^*}{\partial X_j} = (\mathbf{I} - \mathbf{A}^*)^{-1} \frac{\partial\mathbf{G}}{\partial X_j}$$

given that  $(\mathbf{I} - \mathbf{A}^*)^{-1}$  depends only on the geometry and not on the  $X_j$ . The derivative  $\partial\mathbf{G}/\partial X_j$  can be analytically evaluated. Thus, for the outer torso, both  $\Phi (= \Phi^*)$  and  $\partial\Phi/\partial X_j (= \partial\Phi^*/\partial X_j)$  matrices are rapidly obtained at each iteration for the inverse dipole parameters, thereby permitting use of the Levenberg-Marquardt algorithm.



A description of the many studies done using SMD and TMD inverse models is to be found elsewhere [50, 51]. A possible clinical application of the inverse SMD solution in electrocardiography is for noninvasive localization of the accessory pathway tract in the Wolff-Parkinson-White syndrome. In this syndrome, the accessory pathway bridges atria and ventricles, resulting in a pre-excitation of the ventricles. The locus of the SMD during early pre-excitation can possibly serve as an indicator of the site of the accessory pathway [56].

### Multiple-Dipole Inverse Solutions

This solution is based on the premise of an underlying multiple-dipole heart model, with the rationale being that the moment of each inversely-computed dipole will reflect the electrical activity of the region it represents. There has not been much recent work done in inverse electrocardiography with this model, and earlier review papers remain relevant [50, 51].

### Inverse Solutions for Epicardial Potentials

Here, the aim is to compute the epicardial potential distribution from the torso potentials using a torso model that represents the region between epicardium and outer torso. Besides its clinical importance, other benefits are the possibility of direct validation of the inverse solution, provided the epicardial distribution can be measured, and the fact that the effect of the most significant inhomogeneity, namely the intracardiac blood masses, is included implicitly. The effect of inhomogeneities external to the heart, such as the lungs, can also be included, but this has to be done explicitly by including these inhomogeneities in the torso model.

If the theoretical relationship between the  $N$  body surface potentials,  $\Phi_B$ , and the  $M$  epicardial potentials,  $\Phi_H$ , ( $N > M$ ) is given by the linear matrix equation,  $\Phi_B = \mathbf{T}_{BH} \Phi_H$ , one looks again to minimize the sum-squared residual,  $\mathfrak{R} = \|\tilde{\Phi}_B - \mathbf{T}_{BH} \Phi_H\|^2$ . The transfer matrix,  $\mathbf{T}_{BH}$ , may be estimated from a solution to the forward problem, via either a finite-element discretization of the region between epicardial and outer torso surface, or the boundary-element formulation of Eq. (8). The difficulty is that with the large number of epicardial potentials to be computed (usually around 60), the

## An important question with Tikhonov regularization is the optimum choice of the regularization parameter.

inverse problem becomes increasingly ill-posed. This is exemplified by an increased linear dependence among the columns of  $\mathbf{T}_{BH}$ , and a singular or nearly singular  $\mathbf{T}_{BH}^T \mathbf{T}_{BH}$  matrix, so that a solution using the normal Eq. (23) is not possible. All the inverse solutions for epicardial potentials described below invoke explicit constraints on these potentials in order to circumvent this problem.

### Truncated Singular-Value Decomposition

The relation  $\Phi_B = \mathbf{T}_{BH} \Phi_H$  being linear, the dimensionality of the solution space (i.e., the maximum number of independent components in  $\Phi_H$  that can be determined) is equal to the rank of the matrix  $\mathbf{T}_{BH}$ . This rank is most easily determined from a singular-value decomposition (SVD) of the  $N \times M$  matrix  $\mathbf{T}_{BH}$ , given by  $\mathbf{T}_{BH} = \mathbf{U} \mathbf{S} \mathbf{V}^T$ , where  $\mathbf{U}$  and  $\mathbf{V}$  are  $N \times N$  and  $M \times M$  orthogonal matrices, respectively, and  $\mathbf{S}$  is an  $N \times M$  diagonal matrix whose diagonal elements are ordered such that  $s_{11} \geq s_{22} \geq \dots \geq s_{ii} \geq \dots \geq s_{MM} \geq 0$  [57]. These diagonal elements are termed the singular values of  $\mathbf{T}_{BH}$ . The rank of the matrix  $\mathbf{T}_{BH}$  is equal to that of  $\mathbf{S}$  [57], so that if only the first  $r$  singular values are nonzero,  $r$  is also the rank of  $\mathbf{T}_{BH}$ . Accordingly, no more than  $r$  linearly independent solution-components may be determined.

The minimum residual solution of the set of equations  $\tilde{\Phi}_B = \mathbf{T}_{BH} \Phi_H$ , where  $\tilde{\Phi}_B$  denotes the measured body potentials, follows by using the above decomposition to rewrite the set as:

$$\mathbf{U}^T \tilde{\Phi}_B = \mathbf{S} \mathbf{V}^T \Phi_H \quad (24)$$

Now define

$$\begin{aligned} \mathbf{U}^T \tilde{\Phi}_B &= \tilde{\Psi} = \begin{Bmatrix} \tilde{\Psi}_1 \\ \tilde{\Psi}_2 \end{Bmatrix} \begin{matrix} r \\ N-r \end{matrix} \\ \mathbf{V}^T \Phi_H &= \mathbf{Y} = \begin{Bmatrix} \mathbf{Y}_1 \\ \mathbf{Y}_2 \end{Bmatrix} \begin{matrix} r \\ M-r \end{matrix} \end{aligned} \quad (25)$$

where we have partitioned the  $\tilde{\Psi}$  and  $\mathbf{Y}$  vectors as indicated. The individual elements of  $\tilde{\Psi}$  are the projections of the measured surface distribution,  $\tilde{\Phi}_B$ , along the individual columns of  $\mathbf{U}$ , and similarly, the individual elements of  $\mathbf{Y}$  are the projections of the solution  $\Phi_H$  along the columns of  $\mathbf{V}$ . Then, since we know that  $\mathbf{S}$  is diagonal and of rank  $r$ , Eq. (24) yields:

$$\begin{bmatrix} \tilde{\Psi}_1 \\ \tilde{\Psi}_2 \end{bmatrix} = \begin{bmatrix} \mathbf{S}_r & \mathbf{0} \\ \mathbf{0} & \mathbf{0} \end{bmatrix} \begin{bmatrix} \mathbf{Y}_1 \\ \mathbf{Y}_2 \end{bmatrix} \quad (26)$$

A general solution to Eq. (26) is of the form:

$$\mathbf{Y} = \begin{bmatrix} \mathbf{S}_r^{-1} \tilde{\Psi}_1 \\ \mathbf{Y}_2 \end{bmatrix} \quad (27)$$

where  $\mathbf{Y}_2$  is arbitrary and  $\mathbf{S}_r^{-1}$  is easily computed. In scalar form, an individual solution component among the  $\mathbf{Y}_1$  is simply:

$$y_i = \frac{\tilde{\Psi}_i}{s_{ii}} \quad (28)$$

Since noise in the measured surface potentials is reflected in the  $\tilde{\Psi}_i$ , those solution components,  $y_i$ , corresponding to the smallest singular values are going to be the most susceptible to this noise. The epicardial potentials,  $\Phi_H$ , are then, employing Eqs. (27) and (25):

$$\Phi_H = \mathbf{V} \mathbf{Y} = \mathbf{V} \begin{bmatrix} \mathbf{S}_r^{-1} \tilde{\Psi}_1 \\ \mathbf{Y}_2 \end{bmatrix} \quad (29)$$

It can be shown that this is a minimum residual solution [51].

When the rank  $r$  of  $\mathbf{T}_{BH}$  is less than the number of solution components,  $M$ , constraints have to be imposed on these components in order to obtain a unique solution. One simple way to achieve this is by setting  $\mathbf{Y}_2$  in Eq. (29) to zero. Then,  $\Phi_H$  is obtained from:

$$\Phi_H = \mathbf{V} \mathbf{Y} = \mathbf{V} \begin{bmatrix} \mathbf{S}_r^{-1} \tilde{\Psi}_1 \\ \mathbf{0} \end{bmatrix} = \mathbf{V}_r \mathbf{S}_r^{-1} \mathbf{U}_r^T \tilde{\Phi}_B \quad (30)$$

where  $\mathbf{U}_r$ ,  $\mathbf{V}_r$  contain the first  $r$  columns of  $\mathbf{U}$  and  $\mathbf{V}$ , respectively. The accompanying constraints on the solution components of  $\Phi_H$  are obtained from the  $M - r$  relations of:

$$\mathbf{V}^T \Phi_H = \mathbf{Y} = \begin{bmatrix} \mathbf{S}_r^{-1} \tilde{\Phi}_r \\ \mathbf{0} \end{bmatrix} \quad (31)$$

corresponding to the zero values of  $\mathbf{Y}$ . In practice, due to noise (i.e., measurement noise in  $\tilde{\Phi}_B$ , geometry error in determining the matrix  $\mathbf{T}_{BH}$ , as well as numerical discretization errors in the computations), fewer than  $r$  independent components of  $\Phi_H$  can be estimated reliably. Accordingly, to ensure solution stability in the presence of noise, the dimensionality of the solution space is further restricted to  $k < r$  and the smaller singular values from  $s_{k+1,k+1}$  onward are also assumed to be zero. The solution is then again given by Eq. (30), but with the matrices  $\mathbf{U}$ ,  $\mathbf{V}$  and  $\mathbf{S}^{-1}$  truncated after the first  $k$  rather than the first  $r$  columns. Truncated SVD essentially involves a judicious choice of the parameter  $k$  so as to result in a stable, low-residual, solution. By assuming a spherical torso, and performing an SVD of the transfer matrix, Okamoto, et al. [58], concluded that only 15 independent parameters can be computed from surface potentials measured with accuracies as high as 99%.

#### Regularization

An alternative procedure, known as "regularization" [59, 60], uses general information about the solution to constrain it, and thereby increase its stability. The more common regularization constraints employed are minimization either of the norm, of the surface gradient, or of the surface Laplacian of the epicardial potential distribution, and have been termed zero-order, first-order, and second-order Tikhonov regularization, respectively. With regularization, instead of simply minimizing the surface-potential residuals, the function  $\mathfrak{R}_\gamma$  to be minimized is given by:

$$\mathfrak{R}_\gamma = \|\tilde{\Phi}_B - \mathbf{T}_{BH} \Phi_H\|^2 + \gamma \|\mathbf{C} \Phi_H\|^2 \quad (32)$$

where the constraint matrix,  $\mathbf{C}$ , is either an  $M \times M$  identity matrix  $\mathbf{I}$ , a discrete approximation to the spatial gradient; or a discrete approximation to the surface Laplacian in the case of zero-order, first-order, and second-order Tikhonov regularization, respectively. The constant,  $\gamma$ , is termed the "regularization parameter" and controls the weight attributed to the constraint condition. Since minimizing  $\mathfrak{R}_\gamma$  in Eq. (32) is equivalent to the minimum-residual solution of the augmented set of equations:

$$\begin{bmatrix} \tilde{\Phi}_B \\ \mathbf{0} \end{bmatrix} = \begin{bmatrix} \mathbf{T}_{BH} \\ \sqrt{\gamma} \mathbf{C} \end{bmatrix} \Phi_H \quad (33)$$

we may write the normal equation for the solution  $\Phi_H$ , namely:

$$\Phi_H = (\mathbf{T}_{BH}^T \mathbf{T}_{BH} + \gamma \mathbf{C}^T \mathbf{C})^{-1} \mathbf{T}_{BH}^T \tilde{\Phi}_B \quad (34)$$

Little difficulty is encountered with Eq. (34), as a sufficiently large  $\gamma$  will make  $(\mathbf{T}_{BH}^T \mathbf{T}_{BH} + \gamma \mathbf{C}^T \mathbf{C})$  nonsingular and result in a unique, stable solution for  $\Phi_H$ . Since the sum-squared residual (the first term in Eq. (32)) also increases with  $\gamma$ , regularization essentially involves selecting the smallest  $\gamma$  that stabilizes the solution. As it is still by no means clear which of zero-, first-, or second-order Tikhonov regularization is most appropriate for the inverse epicardial potential solution, in the sequel we restrict ourselves to the simpler zero-order situation. It can be shown via the SVD of  $\mathbf{T}_{BH}$  that in zero-order regularization, the solution components are given by:

$$\gamma_i = \frac{\tilde{\Phi}_i}{s_{ii} + (\gamma/s_{ii})} \quad (35)$$

Upon comparing with Eq. (28), this expression shows that as long as  $\gamma$  is not too large, the smaller singular values of  $\mathbf{T}_{BH}$  are, in effect, scaled up in magnitude, contributing to the greater stability of the solution, while the larger ones remain practically unaffected.

An important question with Tikhonov regularization is the optimum choice of the regularization parameter. As  $\gamma$  tends to zero, the solution given by Eq. (34) tends to approach the minimum-residual solution,  $\Phi_H = [\mathbf{T}_{BH}^T \mathbf{T}_{BH}]^{-1} \mathbf{T}_{BH}^T \tilde{\Phi}_B$ , with its accompanying instability and oscillation of epicardial potential magnitudes. For very small values of  $\gamma$ , this oscillation tends to affect the smaller values of epicardial potential particularly, resulting in erratic shifts of the zero isopotential line [61]. Such a solution is termed "under-regularized." On the other hand, large values of  $\gamma$  tend to make the solution overly smooth, since the constraint condition, exemplified by the second term in  $\mathfrak{R}_\gamma$ , dominates (see Eq. (32)). Considerable smoothing of epicardial potential gradients takes place with such an "over-regularized" solution. The optimum value,  $\gamma_{opt}$ , lies between these two extremes, providing a balance between instability and excessive smoothing. If the epicardial potentials are known a priori, as

**Increasingly, the need to impose some form of temporal constraint on the epicardial potentials is being recognized.**

with simulation or experimental studies, we can define  $\gamma_{opt}$  as the parameter that minimizes the relative error,  $RE$ , given by:

$$RE = \sqrt{\sum_{i=1}^M (\tilde{\Phi}_{Hi} - \Phi_{Hi})^2 / \sum_{i=1}^M (\tilde{\Phi}_{Hi})^2} \quad (36)$$

where the  $\tilde{\Phi}_{Hi}$  are the known values of the individual epicardial potentials. However, in clinical tests in humans, the  $\tilde{\Phi}_{Hi}$  are not known, and some other criterion needs to be used to select a value for  $\gamma$  as close to optimum as possible.

Several methods for selecting  $\gamma$  have been proposed in the literature. If the standard deviation of the noise in  $\tilde{\Phi}_B$  is known,  $\gamma$  can be found by means of a so-called "discrepancy technique" [62, 63]. This approach has been investigated by Johnson [64, 65]. Other methods that do not depend on an a priori knowledge of noise levels in  $\tilde{\Phi}_B$  are "generalized cross-validation" and the "maximum likelihood estimator" [66, 67]. Colli Franzone, et al. [68, 69], proposed an empirical approach for determining  $\gamma$  known as "composite residual and smoothing operator" (CRESO), which also did not require a prior knowledge of noise levels and which led to  $\gamma$  values that performed better than those selected via either the generalized cross-validation or maximum-likelihood estimator criteria. The CRESO approach has gained a certain degree of acceptance for the inverse epicardial-potential problem. It estimates  $\gamma_{CRE}$  as the smallest value of  $\gamma (> 0)$  that results in a relative maximum of the function:

# Of particular promise are inverse solutions that employ temporal constraints.

$$C(\gamma) = \|\Phi_H\|^2 + 2\gamma \frac{d}{d\gamma} \|\Phi_H\|^2 \quad (37)$$

where  $\Phi_H$  is the solution for a particular value of  $\gamma$  and is given by Eq. (34) (with  $C$  equal to the identity matrix).

Recently, Hansen [70, 71] has been an advocate of a less empirical "L-curve" approach to determining  $\gamma$ , first described by Miller [72] and by Lawson and Hanson [73]. The L-curve approach involves a plot using a log-log scale of the norm of the solution  $\|\Phi_H\|$  on the ordinate, against the norm of the residual  $\|\tilde{\Phi}_B - T_{BH}\Phi_H\|$  on the abscissa, with  $\gamma$  as a parameter along the resulting curve. As long as the uncorrelated Gaussian noise present in  $\tilde{\Phi}_B$  dominates the correlated geometric noise in  $T_{BH}$ , this curve is in the form of an "L," and the value,  $\gamma_L$ , at the corner of the "L" is selected. At the corner, both  $\|\Phi_H\|$  and  $\|\tilde{\Phi}_B - T_{BH}\Phi_H\|$  simultaneously attain low values, intuitively suggesting a reasonable solution. A numerical algorithm to compute the site of the corner as the point of maximum curvature has been described by Hansen and O'Leary [74]. However, this algorithm is difficult to implement, and Johnston and Gulrajani [75] have proposed a simpler empirical "zero-crossing" choice,  $\gamma_z$ , for  $\gamma$ . In simulations,  $\gamma_z$  as well as  $\gamma_{CRE}$  were both verified to fall in the corner region. However, these same simulations showed that under low measurement-noise conditions,  $\gamma_{opt}$  did not fall in the corner region, in which event neither  $\gamma_L$ ,  $\gamma_{CRE}$ , or  $\gamma_z$  result in an optimum solution.

## Variants of Tikhonov Regularization

Several variants of Tikhonov regularization have been proposed. If some a priori estimate,  $\Phi_p$ , of the desired epicardial potential distribution is known, an approach proposed by Twomey [76] minimizes:

$$\mathfrak{R}_\gamma = \|\tilde{\Phi}_B - T_{BH}\Phi_H\|^2 + \gamma\|\Phi_H - \Phi_p\|^2 \quad (38)$$

with a solution given by:

$$\Phi_H = [T_{BH}^T T_{BH} + \gamma I]^{-1} [T_{BH}^T \tilde{\Phi}_B + \gamma \Phi_p] \quad (39)$$

Note that the success of this method depends on the correctness of the initial estimate,  $\Phi_p$ , since the solution is biased toward this estimate. The best choice of the regularization parameter with Twomey regularization is still an open question.

Another variant of Tikhonov regularization imposes inequality constraints on the individual epicardial potentials  $\Phi_{Hi}$ . Thus, for example, we have as the objective function to be minimized,

$$\mathfrak{R}_\gamma = \|\tilde{\Phi}_B - T_{BH}\Phi_H\|^2 + \gamma\|\Phi_H\|^2, \text{ subject to the additional constraint that } a_i \leq \Phi_{Hi} \leq b_i.$$

Selection of the limiting constraint values  $a_i$  and  $b_i$  can pose a problem with this method, since clearly little improvement is to be expected unless these are tailored to the epicardial distribution at hand. Iakovidis and Gulrajani [77] have described one scheme that exploits experimental observations by Soucy [61] that the under-regularized zero-order Tikhonov solution better preserves regions of high epicardial-potential gradients at the expense of an erratic zero isopotential contour, whereas the over-regularized solution better preserves the position of the zero isocontour at the expense of smoothing the high gradients. In an effort to combine the better features of both under- and over-regularized solutions, they proposed a two-pass approach, first selecting an over-regularized solution, and next a final under-regularized solution subject to constraints that fixed its zero isopotential to that observed in the earlier over-regularized solution.

Oster and Rudy [78] have suggested that a particular epicardial map can be separated into component maps with different spatial characteristics, with each component recovered using different degrees of regularization. In concept, this is similar to Iakovidis and Gulrajani's two-pass scheme, in which the first over-regularized pass fixes the zero isopotential region and the subsequent under-regularized pass the rest. However, Oster and Rudy formalized this notion by proposing that the potential distributions

be split using SVD. Employing the SVD,  $T_{BH} = USV^T$ , and writing  $\tilde{\Psi} = U^T \tilde{\Phi}_B$  and  $Y = V^T \Phi_H$ , we see from Eq. (28) that each solution component,  $y_i$ , is determined uniquely by its corresponding  $\tilde{\Psi}_i$ . Thus, if the measured body-surface distribution is decomposed into its  $\tilde{\Psi}_i$  components, each component can be separately regularized using its own optimal regularization parameter,  $\gamma_i$ , to obtain the individual  $y_i$  distributions. The final epicardial solution is obtained from  $\Phi_H = VY$ . Since the higher-order (i.e., the smaller magnitude) SVD components of  $V$  exhibit higher spatial frequencies, this approach represents a regularization based on epicardial spatial frequencies.

## Epicardial Solutions via Multipoles

Inverse epicardial solutions can also be obtained by first determining an inverse solution in terms of multipoles [79]. The multipole series,  $X$ , is then used in a forward solution (employing Eq. (3)) to compute epicardial potentials, usually on a spherical surface surrounding the epicardium, in order to avoid questions of convergence and precise determinations of epicardial geometry. In effect, we obtain the relationship  $\Phi_H = T_{HX}X$ , where  $T_{HX}$  denotes the transfer matrix between multipoles and epicardial potentials. The multipole series can often be determined directly from the normal Eq. (23), although if hexadecapole terms are desired, some form of regularization is needed. Beetner [80] has suggested using a constraint matrix based on the expected signal power of each multipole component, or even one that minimizes the norm of the epicardial potentials  $\|T_{HX}X\|$ . In the latter situation, the objective function to be minimized is  $\mathfrak{R}_\gamma = \|\tilde{\Phi}_B - TX\|^2 + \gamma\|T_{HX}X\|^2$ .

In simulation studies with the eccentric-spheres model, he obtained more accurate estimates of epicardial potentials with this two-step route than with a conventional one-step zero-order Tikhonov regularization solution for  $\Phi_H$ .

## Other Approaches

Other approaches to the inverse epicardial-potential problem that deserve mention are listed here. The first is a statistical approach based on Wiener filtering that makes use of the covariance matrices characterizing surface-potential noise and epicardial potentials [81]. While this was the first epicardial solution

proposed, the covariance matrices were assumed proportional to the identity matrix, in effect reducing it to zero-order Tikhonov regularization. A more recent epicardial potential solution proposed by Throne and Olson [82, 83] employs a finite-element representation of the forward problem and obtains the epicardial distribution as a linear combination of epicardial eigenvectors. Still another employs a forward solution for the surface Laplacian as the transfer matrix [84-86]. A final approach [87] solves for *both* epicardial potentials and gradients by writing Equations (6) and (7) in matrix form as follows:

$$\begin{bmatrix} \mathbf{A}_{BH} & \mathbf{B}_{BH} \\ \mathbf{A}_{HH} & \mathbf{B}_{HH} \end{bmatrix} \begin{bmatrix} \Phi_H \\ \Gamma_H \end{bmatrix} = \begin{bmatrix} -\mathbf{A}_{BB} \\ -\mathbf{A}_{HB} \end{bmatrix} \tilde{\Phi}_B \quad (40)$$

Horáček and Clements [88] have successfully tested this approach via simulation and list three advantages for it. First, knowing epicardial potential gradients normal to the surface (and hence the normal current density) enables a better appreciation of the underlying injury current sources that arise in the ischemic heart. Second, although the coefficient matrix on the left-hand-side in Eq. (40) is larger, it is less ill-conditioned than the more conventional  $\mathbf{T}_{BH}$  matrix of Eq. (8). Finally, the input vector to the inverse calculations

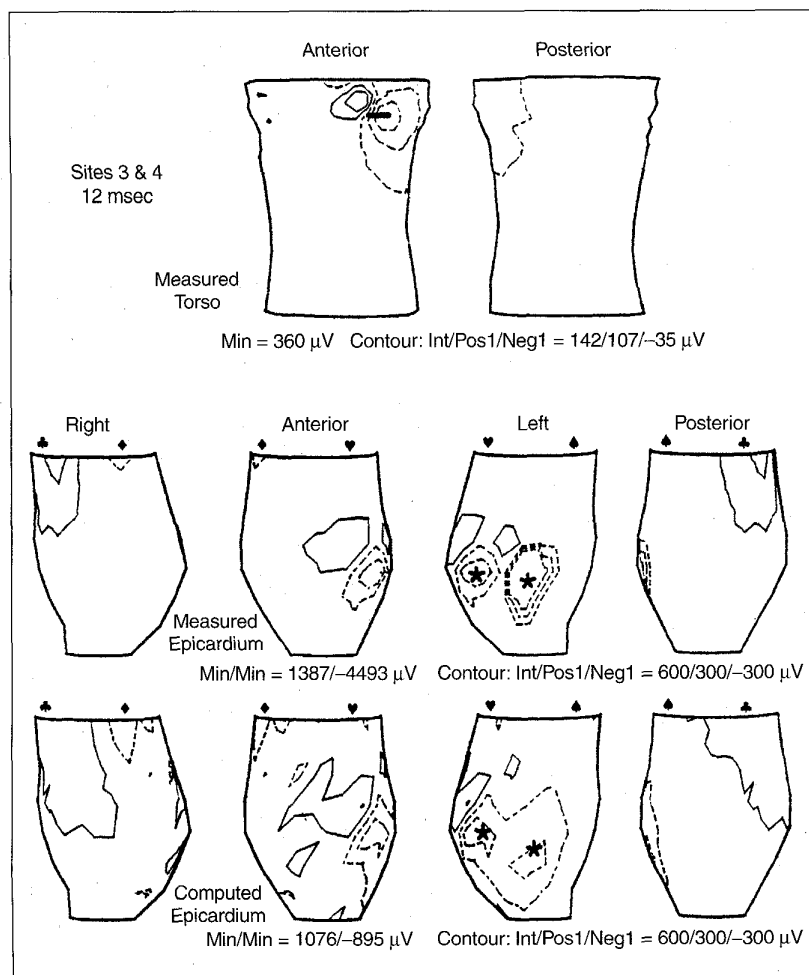
in Eq. (40) is no longer the directly measured, and therefore noisy, body-surface potentials  $\tilde{\Phi}_B$ , but is a *filtered* version of these potentials because  $\tilde{\Phi}_B$  is multiplied by the coefficient matrix on the right side.

#### Imposing Temporal Constraints

None of the inverse epicardial solutions described above exploit the temporal correlation that must exist between epicardial potentials at adjacent time instants. Instead, the epicardial distribution at each time instant is obtained in independent fashion from the body-surface distribution at that time instant alone. Increasingly, the need to impose some form of temporal constraint on the epicardial potentials is being recognized. An initial effort was made by Oster and Rudy [89] using Twomey regularization, with  $\Phi_p$  taken as a *predicted* value for the desired epicardial distribution,  $\Phi_H^{(j)}$ , at the time instant,  $j$ , under consideration. This predicted value can be obtained from a forward interpolation using the epicardial distributions at the two prior sampling instants,  $j-1$  and  $j-2$ , according to the equation  $\Phi_p = 2\Phi_H^{(j-1)} - \Phi_H^{(j-2)}$ . This scheme was successfully tested with an isolated dog-heart preparation placed in a plexiglass human torso, in which both torso and epicardial surface potentials were known. Its extension to the clinical situation where epicardial potentials are unknown is somewhat problematic.

A second approach was described by Brooks, et al. [90-91], who, in addition to spatial constraints on the epicardial potential distribution, proposed a temporal constraint matrix akin to minimizing the time derivative of the epicardial potentials. An additional regularization constraint (with a second regularization parameter) that incorporates this temporal derivative constraint can be introduced in Eq. (32). Now, however, a global solution is sought over space as well as over time; e.g., during the activation (or QRS) interval. This is a much more difficult problem since the matrix dimensions are larger and there are two regularization parameters to be determined. Brooks, et al., have reported some initial work with this combined time and space regularization, showing also how the two regularization parameters can be determined using an *L-surface*.

Most recently, Greensite [92] has proposed a combined time-space regularization of the temporal sequence of  $N$ ,



4. Inverse solutions obtained employing an isolated dog-heart inside a torso-shaped tank. The top row shows anterior and posterior views of the torso surface potentials obtained 12 msec after pacing at epicardial sites 3 and 4 (approximately 17 mm apart). The middle row shows four views of the measured epicardial potential distribution, and the bottom row the corresponding inversely calculated epicardial distribution. The asterisks indicate the actual pacing sites in the measured maps and the inferred ones (in the centers of the regions of negativity) in the computed maps. Zero-order Tikhonov regularization with regularization parameter  $\gamma_{CRE}$  was used. (Reproduced from [96], with permission from Williams and Wilkins.)

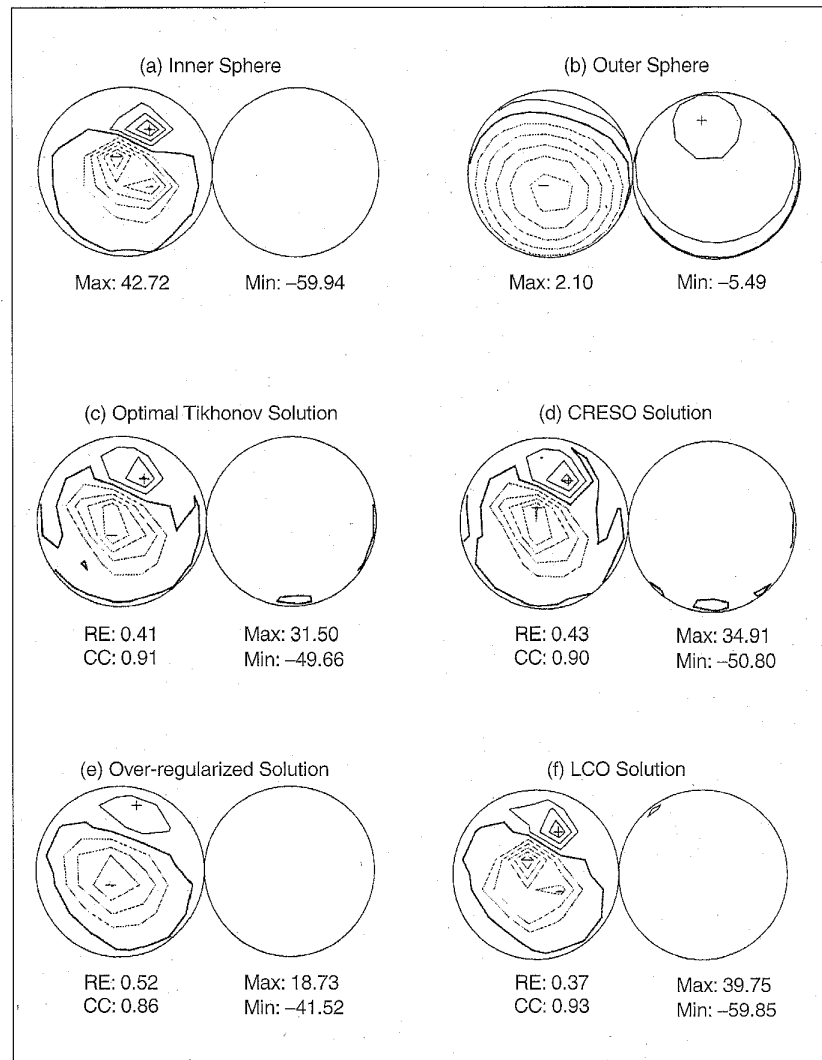
body-surface potential distributions recorded during an activation cycle. The forward relation is again  $\Phi_B = T_{BH} \Phi_H$ , but where  $\Phi_B$  and  $\Phi_H$  are now matrices of dimensions  $N \times N_t$  and  $M \times N_t$ , respectively. The standard approach then involves solving each column of the recorded  $\tilde{\Phi}_B$  matrix for the corresponding column of  $\Phi_H$ . Greensite suggests that a better approach is to first perform an SVD of the  $\tilde{\Phi}_B$  matrix, so that we get  $\tilde{\Phi}_B = \tilde{U}_B \tilde{S}_B \tilde{V}_B^T$ , where  $\tilde{U}_B$ ,  $\tilde{S}_B$ , and  $\tilde{V}_B$  are now  $N \times N$ ,  $N \times N_t$ , and  $N_t \times N_t$  matrices, respectively. The columns of  $\tilde{U}_B$  then constitute a spatial basis for  $\tilde{\Phi}_B$ . This set of basis functions (each multiplied by their corresponding singular values taken from  $\tilde{S}_B$ ) when solved individually results in corresponding epicardial distributions that may be arranged in an  $M \times N$  matrix,  $\Phi_H$  (assuming  $N_t > N$ ). The final solution for the entire  $M \times N_t$  epicardial matrix,  $\Phi_H$ , is obtained as  $\Phi_H = \Phi_H \tilde{V}_B^T$ , where only the first  $N$  rows of  $\tilde{V}_B^T$  are taken. The big advantage of this procedure is that those columns of  $\tilde{U}_B$  (corresponding to the smaller singular values of  $\tilde{S}_B$ ) that largely represent noise in the  $\tilde{\Phi}_B$  distribution may be discarded, and Greensite shows how to identify the cut-off point. In effect, only the first  $n$  columns of  $\tilde{U}_B$  need be considered, where  $n$  is much less than  $N$  (and hence  $N_t$ ). Besides reducing the number of inverse solutions needed, Greensite's approach simultaneously performs a noise filtering of the data. Furthermore, each selected column of  $\tilde{U}_B$  is solved with its own customized SVD truncation index or regularization parameter, depending on the stabilizing method chosen.

A completely different approach that combines time-space regularization [93-94] assumes that the temporal evolution of the epicardial potentials from one instant to the next is governed by a linear prediction equation. Kalman filtering techniques are then used to reconstruct the epicardial potentials.

Finally, time-space regularization of the inverse epicardial potential problem can also be achieved via convex optimization. Here any number of constraints, spatial as well as temporal, are used to restrict the solution to a closed convex set in epicardial space. The solution found is only required to be admissible among the

many possible solutions that meet all the constraints. There is no regularization needed and no criterion of optimality. The correctness of the solution is guided

by the appropriateness and the efficacy of the constraints used. Ahmad, et al. [95], describe an initial simulation study with this approach.



5. (a) Analytically calculated inner sphere distribution due to three radial dipoles, one oriented outward and two inward, located within the inner of two concentric spheres of radius 4 and 10 cm, respectively. (b) Outer-sphere distribution for the same setup. (c) Zero-order Tikhonov solution obtained from the outer-sphere distribution in (b), employing regularization parameter  $\gamma_{opt}$ . (d) Zero-order Tikhonov solution employing  $\gamma_{CRE}$ . (e) First-pass overregularized solution that was used to fix the zero isocontour in a two-pass approach to improving Tikhonov regularization. (f) Final under-regularized pass. Each circle represents the projection of one hemisphere. Potential values are in arbitrary units. The isocontours are spaced at 10 unit intervals for (a), (c)-(f), and at 1 unit intervals for (b), with the zero isocontour identified by the bold trace. The positions of all extrema (principal and secondary) are marked, with the values of the principal extrema indicated below each distribution. In addition, the values of the relative error (RE) and the correlation coefficient (CC) between the inner-sphere distribution of (a) and each of the solutions (c)-(f) are given below the respective solutions. All solutions were computed using a transfer matrix that corresponds to the geometry of the inner sphere displaced by 0.5 cm so as to introduce geometric noise. Figure modified from [77], with permission from Elsevier Science.

### Examples of Inverse Epicardial Potential Solutions

The first example illustrates results obtained with an isolated dog-heart preparation placed inside an electrolyte-filled torso-shaped tank, thereby permitting recording of both torso and epicardial potentials [96]. The latter were measured in the electrolyte at known positions near the epicardial surface. Figure 4 depicts the torso, measured epicardial, and inversely computed epicardial distributions following simultaneous pacing from two sites 17 mm apart on the left epicardium. The results show that, in this setup, with geometry errors in  $T_{BH}$  absent, pacing sites could be identified to within 10 mm or better using zero-order Tikhonov regularization.

The second example (Fig. 5), drawn from our own work, depicts the ability of two-pass regularization to improve upon optimal Tikhonov regularization. Three dipoles inside a sphere surrounded by a second concentric sphere gave rise to the "epicardial" and "body" surface distributions (Figs. 5(a) and 5(b), respectively). Zero-order Tikhonov solutions with regularization parameters  $\gamma_{opt}$  and  $\gamma_{CRE}$  are shown in Figs. 5(c) and 5(d), respectively. By fixing a narrow interval about the zero isocontour in the first-pass over-regularized solution of Fig. 5(e), we were able to obtain a final under-regularized solution (Fig. 5(f)) that picked up the secondary minimum in the original distribution (Fig. 5(a)). Later research [97] has identified a problem with this approach if epicardial potential distributions with high-gradient regions clustered on either side of the zero isopotential are to be recovered. Constraints around the zero isopotential based on an overregularized solution can then compromise the final solution. It would be interesting to see if Oster and Rudy's approach [78] of individually regularizing the different spatial components of such a high-gradient epicardial distribution would circumvent this problem.

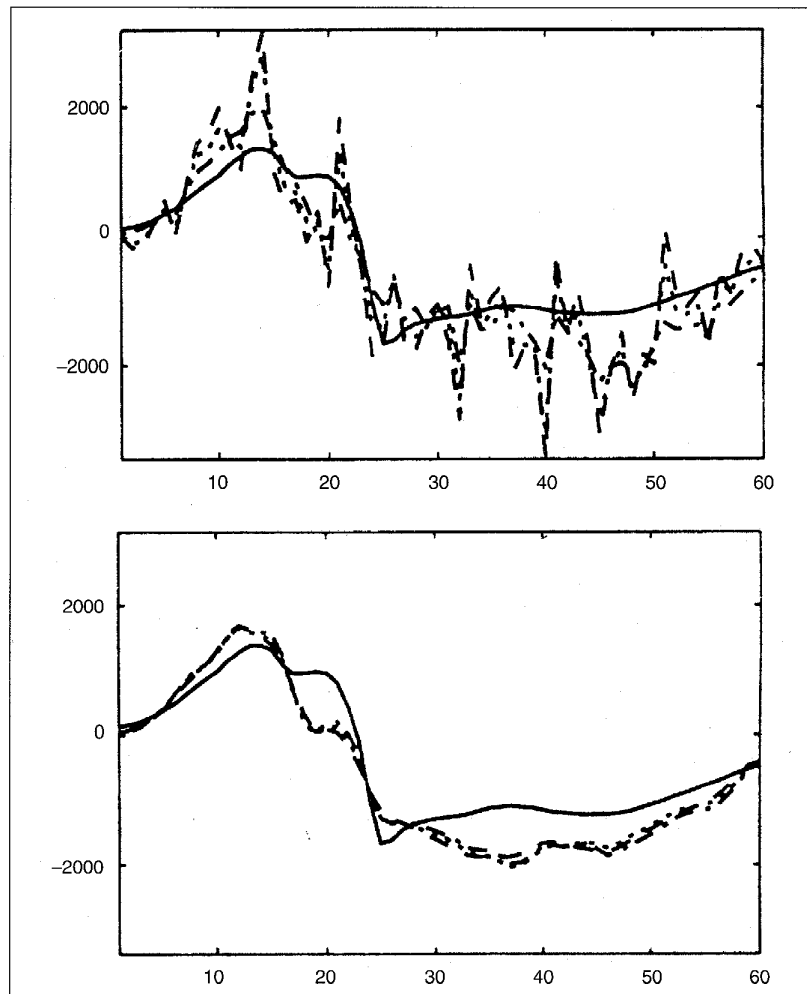
The final example focuses on the ability of temporal regularization to achieve temporal smoothing of the inversely computed epicardial potential. Figure 6 (top) shows a measured epicardial potential waveform, together with epicardial potential waveforms computed using just spatial regularization at individual time instants. In Figure 6 (bottom), much smoother epicardial waveforms obtained with the two-regularization-parameter time-space approach of Brooks, et al., [90-91] are

shown. A similar degree of smoothing has also been demonstrated by Greensite and Huiskamp [98] using Greensite's [92] time-space regularization approach.

### Inverse Determination of Heart-Surface Isochrones

Rather than characterize the electrical activity of the heart by dipoles or epicardial potentials, this inverse solution sets out to determine the activation isochrones at the heart's surface. It is based on the assumption that the activation isochrones can be represented by a uniform layer of dipoles normal to the isochrone surface and pointing toward as yet undepolarized

tissue. This representation is equivalent to one characterizing the depolarized surface of both the epicardium and the endocardium by a layer of dipoles of the same uniform strength and normal to these surfaces, but pointing towards depolarized tissue, since the difference between these two representations is a closed uniform-dipole layer that generates no external potential. Inverse determination of surface isochrones essentially involves the determination of the extent of these epicardial and endocardial dipole layers at successive instants during depolarization, from the torso potentials and the torso as well as heart geometry. Put another way, the *acti-*



6. Comparison of spatial (top) and combined temporal-spatial (bottom) regularization. In each panel, the solid trace represents a measured epicardial waveform for 60 msec during QRS, the other traces are inversely computed waveforms with various regularization parameters. The measured epicardial waveforms, which were obtained from an isolated dog heart, were used to simulate torso ECGs, from which, after the addition of measurement noise, the inverse epicardial waveforms were computed. The temporal smoothing achieved by time-space regularization is evident. (Reproduced, with permission, from [52]. Copyright 1998 IEEE.)

vation times of the epicardial and endocardial surfaces are obtained. The problem was first studied by Cuppen and van Oosterom [99, 100].

If  $T(y, x)$  represents the forward transfer coefficient relating the potential  $\Phi_B$  at a body-surface point,  $y$ , to the uniform dipole element at  $x$ , then Cuppen and van Oosterom show that:

$$A_B(y) = - \int_{S_H} T(y, x) \tau(x) dx \quad (41)$$

where  $A_B(y)$  is the time-integral during the QRS interval of the torso potential  $\Phi_B$  at site  $y$ ,  $\tau(x)$  is the desired activation time at site  $x$ , and  $S_H$  represents both the endocardial and epicardial surfaces. Cuppen and van Oosterom [100] applied Eq. (41) in simulation studies with numerical models of the heart and torso. They first transposed the isolated-heart activation data of Durrer, et al. [15], to their heart model (Fig. 7(a)). Next,  $T(y, x)$  was estimated using the integral equation for the potential (Eq. (1)) and used in conjunction with the activation data to calculate the torso potentials. These were then contaminated with random noise prior to being integrated over the QRS duration to obtain  $A_B(y)$ . Finally, the Durrer data (i.e.,  $\tau(x)$ ) was inversely computed from  $A_B(y)$  using a discrete form of Eq. (41) and employing a variant of truncated SVD. Figure 7(b) plots the recovered epicardial isochrones, when the added random noise was 1% of the maximum surface potential. Cuppen and van Oosterom found that while normal signal noise was not critical, errors in geometry and conductivity between forward and inverse torso models were much more so. Finally, epicardial isochrones were recovered with greater accuracy than endocardial ones.

Cuppen and van Oosterom point out that the spreading of the surface activation isochrones is an inherently smooth process. Therefore, the use of regularization constraints is more apt than it would be, say, for the inverse calculation of epicardial potentials, where sharp gradients are present. On the other hand, the method relies on the uniform-dipole-layer concept and is, therefore, not applicable where this does not hold, as is the case for anisotropic myocardium, where a nonuniform dipole layer oblique to the wavefront is more appropriate [101]. Similarly, in cases of old myocardial infarction, application of the method requires a knowledge of the infarct geometry, which, in effect, forms a boundary surface for the

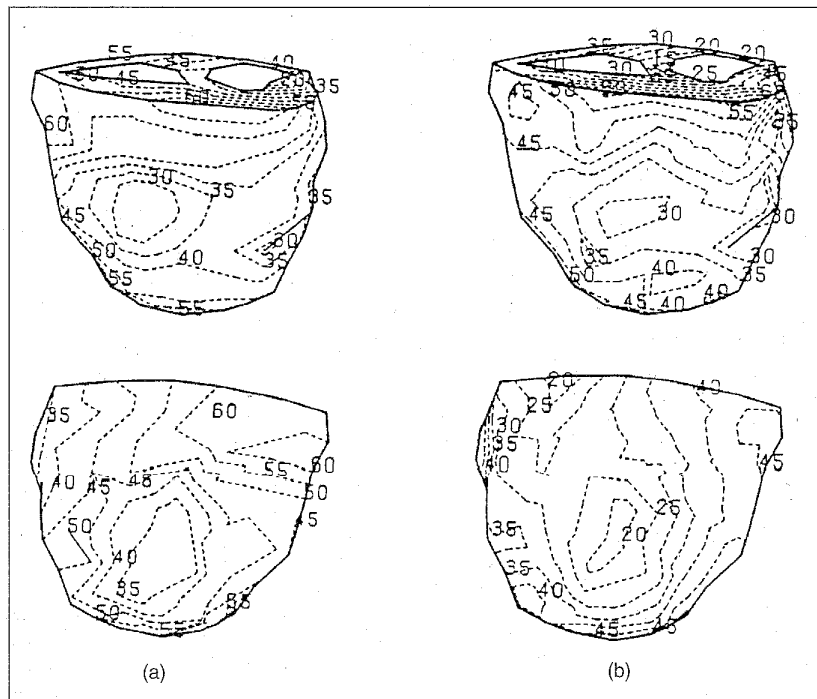
heart. This inverse solution for activation isochrones is, accordingly, best suited for the study of ectopic beats and other rhythm disturbances. Interesting extensions of the method that employ second-order Tikhonov regularization have been described by Huiskamp and van Oosterom [102-104] and used by them to investigate the effects of torso geometry and heart position on the inverse solution.

A completely different approach to obtaining the surface activation isochrones, valid in principle even with anisotropic myocardium and the oblique-dipole model, has been proposed by Greensite [105, 106]. The basic objective here is to locate the "critical points" of the activation map on the heart surface. These critical points,  $x_c$ , are the extrema sites (i.e., minima, maxima or saddle points) on the map of heart-surface activation times. Thus, the epicardial breakthrough of the transmural wavefront arriving from the endocardium is identified by a minimum in the epicardial activation map, sites where the epicardial wavefront dies out would be a maximum, and a collision of two epicardial wavefronts would constitute a saddle point. Greensite argues that the "hole" developed in the propagating transmural wavefront when it intersects the

epicardial surface will result in a changed slope in the temporal ECG, leading to a step discontinuity or "jump" in the first derivative of the ECG. The times of these discontinuities identifies the "critical times" associated with the critical points. Greensite [106] has shown that the magnitude of the jump,  $J(y)$ , in the derivative of the potential at a body site,  $y$ , is given by:

$$J(y) \propto \frac{2\pi v}{\sqrt{C}} \mathbf{p}(x_c) \cdot \nabla \left( \frac{1}{r(x_c, y)} \right) \quad (42)$$

where  $\mathbf{p}(x_c)$  is the current dipole density (uniform or oblique) associated with the wavefront at the breakthrough site,  $x_c$ ;  $v$  is the wavefront velocity;  $C$  is a measure of the curvature difference between wavefront surface and epicardial surface at  $x_c$ ; and  $r(x_c, y)$  the distance between  $x_c$  and  $y$ . Note that Eq. (42) describes a dipole field, and Greensite [106] argues that an SMD solution from a "jump map," namely the distribution on the body surface of the jump magnitudes in the potential derivatives at a given critical time, would locate the corresponding critical point,  $x_c$ , on the epicardium. In a subsequent step, these critical points could serve as a priori data to constrain appropriately a full activation-isochrone solution.



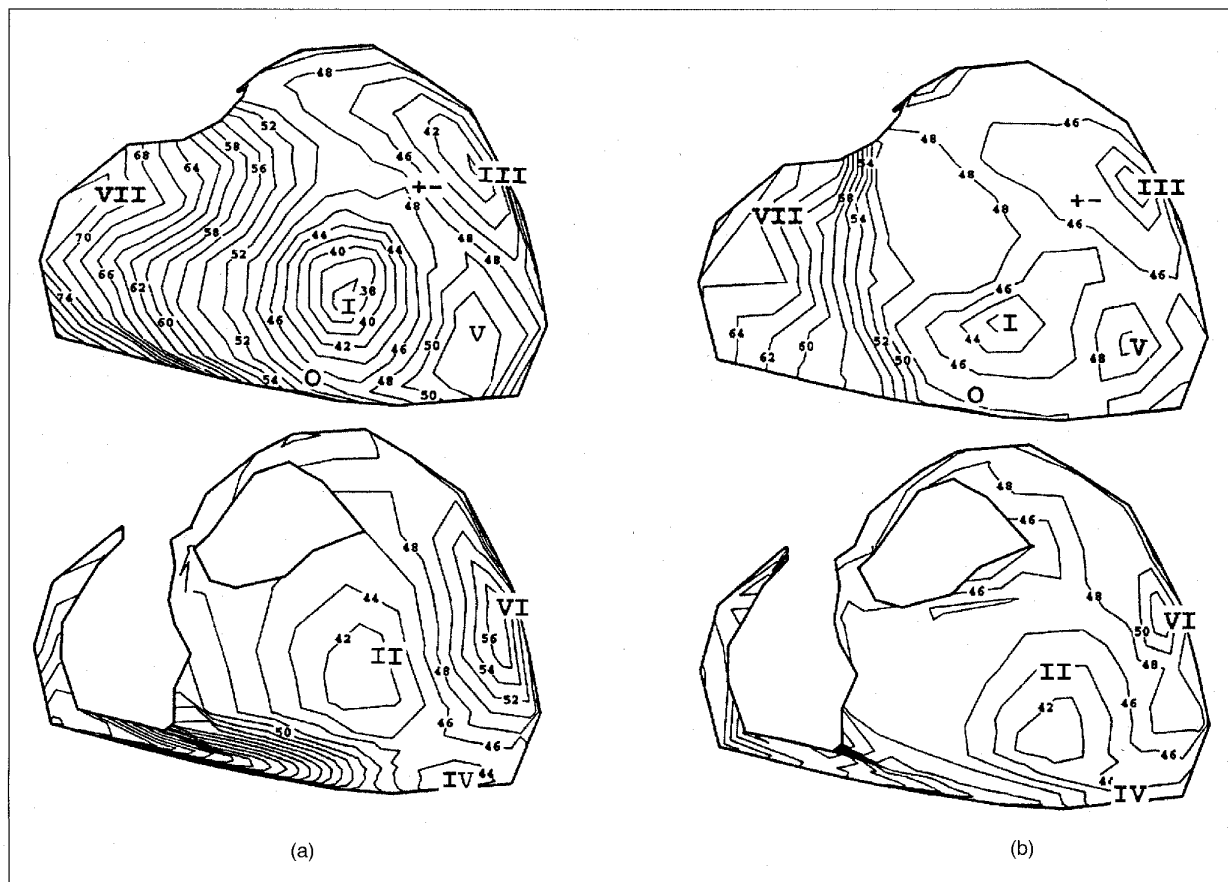
7. Inverse recovery of heart-surface isochrones. (a) Anterior (top) and posterior (bottom) views of the starting epicardial-surface activation isochrones plotted on an upright model heart. (b) Corresponding views of the inversely computed isochrones. (Reproduced, with permission, from [100]. Copyright 1984 IEEE.)



A more recent theorem by Greensite [107] has obviated the need to measure jumps in the first derivative of the ECG potentials. This theorem states that  $x_c$  is a critical point, with a critical time in the interval  $[0, t]$ , if and only if the transfer function  $T(y, x_c)$  associated with this point is contained in the spatial signal space of the body-surface potentials during the interval  $[0, t]$ . Note that in the discrete situation,  $T(y, x_c)$  defines a vector since  $y$  spans all body-surface points. The spatial signal space of the measured body-surface potentials,  $\tilde{\Phi}_B$ , during QRS is obtained from the matrix  $\tilde{U}_B$  of the SVD of the  $N \times N$  matrix,

$\tilde{\Phi}_B$ , namely  $\tilde{\Phi}_B = \tilde{U}_B \tilde{S}_B \tilde{V}_B^T$ . Huiskamp and Greensite [108] suggest criteria for identifying the effective rank  $k$  of  $\tilde{\Phi}_B$  such that columns 1, ...,  $k$ , of  $\tilde{U}_B$  are associated largely with signal space and the rest largely with noise. The vector representing the transfer function  $T(y, x_c)$  of each epicardial point is tested via the multiple signal classification (MUSIC) method of antenna theory [109] for its distance from this signal space. Epicardial sites where the reciprocal of this distance is large indicate critical points. The critical times associated with each critical point is found by repeating this test of the transfer function  $T(y, x_c)$  of each critical

point, with the time interval,  $t$ , gradually increased from zero. In other words, the test is performed repeatedly using successive  $\tilde{U}_B$  matrices determined from only the first two columns of  $\tilde{\Phi}_B$ , the first three columns of  $\tilde{\Phi}_B$ , and so on. The critical time is found when the reciprocal distance first jumps to a large value and remains there for the rest of QRS. (In practice, a slightly more sophisticated test function than just the reciprocal distance is used to identify critical times at each epicardial site.) Once these critical times and sites are identified, they can be used as before to constrain a full activation-isochrone solution. Simulation tests



**8. Inverse recovery of critical points.** (a) Anterior (top) and posterior (bottom) views of the starting epicardial-surface activation isochrones plotted at steps of 2 msec on a model heart oriented as in the torso. Note that, unlike in Fig. 7, the posterior view is that of the posterior wall, but seen from an anterior perspective. Labels I-IV indicate breakthrough sites, V-VII sinks, +- a collision site, and O a noncritical point. These epicardial isochrones together with endocardial ones (not shown here) were used to generate surface potentials, from which, after the addition of measurement noise, the critical points were inversely obtained. (b) Inversely computed critical points. Note that the positions of the labels are the same as those in (a) and serve to indicate the correct solution. Only the location and critical times of the breakthrough sites, sinks, and collision sites are of significance in (b), as the depicted isochrones constitute just a first approximation to the starting isochrones. Of the breakthrough sites, I is correctly located but with a later critical time, II is incorrectly located but accurate with respect to time, III is accurate with respect to both location and time, and IV is completely missed. Of the sinks, V and VI are accurate, and VII fairly accurate, with respect to both location and time. There is a small positional error in the collision site, +-, but not in the collision time. Critical sites on the endocardium could not be identified. (Reproduced, with permission, from [108]. Copyright 1997 IEEE.)

have shown that the method works quite well in locating critical sites and times on the epicardium (Fig. 8), but not so on the endocardium.

### Future Trends

The availability of more powerful computer workstations will lead to more detailed finite-difference, finite-element, and finite-volume models of the torso and its inhomogeneities, and consequently more accurate solutions to the forward problem of electrocardiography. This, in turn, will also improve inverse solutions. Of particular promise are inverse solutions that employ temporal constraints, either in implicit fashion, such as in the inverse determination of heart-surface isochrones, or in explicit fashion during the inverse determination of epicardial potentials. It remains to be seen whether this promise will be fulfilled in the very near future.

### Acknowledgments

The author thanks Fred Greensite and Rob MacLeod for providing him with pre-publication copies of their recent papers, and Daryl Beetner for a copy of his D.Sc. dissertation. He is also grateful to John Wiley & Sons, Inc. for permission to reuse part of the material in Reference [2]. Work supported by the Natural Sciences and Engineering Research Council of Canada.

Ramesh Gulrajani received a Ph.D. degree in Electrical Engineering from Syracuse University, NY, in 1973. He has been with the Université de Montréal since 1973, where he is now a Professor in the Institute of Biomedical Engineering. His current research interests are in computer models of the heart, and in the forward and inverse problems of electrocardiography and electroencephalography.

**Address for Correspondence:** Ramesh M. Gulrajani, Research Center, Sacré-Coeur Hospital, 5400 Boulevard Gouin West, Montreal, Quebec H4J 1C5, Canada. Tel: (514) 338-2222 Ext. 2499. Fax: (514) 338-2694. E-mail: gulrajani@crhsc.umontreal.ca

### References

1. Yamashita Y: Theoretical studies on the inverse problem in electrocardiography and the uniqueness of the solution. *IEEE Trans Biomed Eng* 29: 719-725, 1982.

2. Gulrajani RM: *Bioelectricity and Biomagnetism*. Wiley, New York, 1998, chapter 7.
3. Barr RC, Pilkington TC, Boineau JP, Spach MS: Determining surface potentials from current dipoles with application to electrocardiography. *IEEE Trans Biomed Eng* 13: 88-92, 1966.
4. Oostendorp TF, van Oosterom A: Source parameter estimation in inhomogeneous volume conductors of arbitrary shape. *IEEE Trans Biomed Eng* 36: 382-391, 1989.
5. Purcell CJ, Stroink G: Moving dipole inverse solutions using realistic torso models. *IEEE Trans Biomed Eng* 38: 82-84, 1991.
6. Barr RC, Ramsey M, III, Spach MS: Relating epicardial to body surface potential distributions by means of transfer coefficients based on geometry measurements. *IEEE Trans Biomed Eng* 24: 1-11, 1977.
7. Meijls JWH, Weier OW, Peters MJ, van Oosterom A: On the numerical accuracy of the boundary element method. *IEEE Trans Biomed Eng* 36: 1038-1049, 1989.
8. Heller L: Computation of the return current in encephalography: the auto solid angle. In: Gmitro AF, Idell PS, LaHaie JJ (Eds.): *Digital Image Synthesis and Inverse Optics*, Proc. SPIE 1351, pp. 376-390, 1990.
9. Walker S, Kilpatrick D: Forward and inverse electrocardiographic calculations using resistor network models of the human torso. *Circ Res* 61: 504-513, 1987.
10. Huebner KH, Thornton EA: *The Finite-Element Method for Engineers*, 2nd ed., Wiley, New York, 1982.
11. Abboud S, Eshel Y, Levy S, Rosenfeld M: Numerical calculation of the potential distribution due to dipole sources in a spherical model of the head. *Comput Biomed Res* 27: 441-455, 1994.
12. Rosenfeld M, Tanami R, Abboud S: Numerical solution of the potential due to dipole sources in volume conductors with arbitrary geometry and conductivity. *IEEE Trans Biomed Eng* 43: 679-689, 1996.
13. Stanley PC, Pilkington TC: The combination method: A numerical technique for electrocardiographic calculations. *IEEE Trans Biomed Eng* 36: 456-461, 1989.
14. Pullan A: A high-order coupled finite element/boundary element torso model. *IEEE Trans Biomed Eng* 43: 292-298, 1996.
15. Durrer D, van Dam RT, Freud GE, Janse MJ, Meijler FL, et al: Total excitation of the isolated human heart. *Circulation* 41: 899-912, 1970.
16. Miller, WT, III, Geselowitz DB: Simulation studies of the electrocardiogram. I. The normal heart. *Circ Res* 43: 301-315, 1978.
17. Okajima M, Fujino T, Kobayashi T, Yamada K: Computer simulation of the propagation process in excitation of the ventricles. *Circ Res* 23: 203-211, 1968.
18. Solomon JC, Selvester RH: Myocardial activation sequence simulation. In: Hoffman I (Ed): *Vectorcardiography* 2, North-Holland Publishing Company, Amsterdam, pp 175-182, 1971.
19. Solomon JC, Selvester RH: Simulation of measured activation sequence in the human heart. *Am Heart J* 85: 518-523, 1973.

20. Horacek BM, Ritsema van Eck HJ: The forward problem of electrocardiography. In: Rijlant P (Ed): *The Electrical Field of the Heart*, Presse Acad Eur, Bruxelles, p 228, 1972.
21. Horacek BM: Digital model for studies in magnetocardiography. *IEEE Trans Magnetics* 9: 440-444, 1973.
22. Eifler WJ, Macchi E, Ritsema van Eck HJ, Horacek BM, Rautaharju PM: Mechanism of generation of body surface electrocardiographic P-waves in normal, middle, and lower sinus rhythms. *Circ Res* 48: 168-182, 1981.
23. Lorange M, Gulrajani RM: A computer heart model incorporating myocardial anisotropy. I. Model construction and simulation of normal activation. *J Electrocardiol* 26: 245-261, 1993.
24. Lorange M, Gulrajani RM, Nadeau RA, Prêda I: A computer heart model incorporating myocardial anisotropy. II. Simulations of conduction block. *J Electrocardiol* 26: 263-277, 1993.
25. Xu Z, Gulrajani RM, Molin F, Lorange M, Dubé B, et al: A computer heart model incorporating anisotropic propagation. III. Simulation of ectopic beats. *J Electrocardiol* 29: 73-90, 1996.
26. SippensGroenewegen A, Spekhorst H, van Hemel NM, Kingma H, Hauer RNW et al: Body surface mapping of ectopic left and right ventricular activation. QRS spectrum in patients without structural heart disease. *Circulation* 82: 879-896, 1990.
27. Dubé B, Gulrajani RM, Lorange M, LeBlanc A-R, Nasimith J, et al: A computer heart model incorporating anisotropic propagation. IV. Simulation of regional myocardial ischemia. *J Electrocardiol* 29: 91-103, 1996.
28. Brody DA: A theoretical analysis of intracavitary blood mass influence on the heart-lead relationship. *Circ Res* 4: 731-738, 1956.
29. Rudy Y, Plonsey R, Leibman J: The effects of variations in conductivity and geometrical parameters on the electrocardiogram, using an eccentric spheres model. *Circ Res* 44: 104-111, 1979.
30. Rudy Y, Plonsey R: A comparison of volume conductor and source geometry effects on body surface and epicardial potentials. *Circ Res* 46: 283-291, 1980.
31. Gulrajani RM, Mailloux GE: A simulation study of the effects of torso inhomogeneities on electrocardiographic potentials, using realistic heart and torso models. *Circ Res* 52: 43-56, 1983.
32. Barnard ACL, Duck IM, Lynn MS: The application of electromagnetic theory to electrocardiology. II. Numerical solution of the integral equations. *Biophys J* 7: 463-491, 1967.
33. Selvester RH, Solomon JC, Gillespie TL: Digital computer model of a total body electrocardiographic surface map. An adult male-torso simulation with lungs. *Circulation* 38: 684-690, 1968.
34. Horacek BM: The Effect on Electrocardiographic Lead Vectors of Conductivity Inhomogeneities in the Human Torso. PhD thesis, Dalhousie Univ, Halifax, Canada, 1971.
35. Johnson CR, MacLeod RS, Ershler PR: A computer model for the study of electrical current flow in the human thorax. *Comput Biol Med* 22: 305-323, 1992.

36. Klepfer RN, Johnson CR, Macleod RS: The effects of inhomogeneities and anisotropies on electrocardiographic fields: A 3-D finite-element study. *IEEE Trans Biomed Eng* 44: 706-719, 1997.
37. Hyttinen J, Kauppinen P, Kõöbi T, Malmivuo J: Importance of the tissue conductivity values in modelling the thorax as a volume conductor. *Proc 19th Internat Conf IEEE Eng Med Biol Soc*, IEEE Press, New York, pp. 2082-2085, 1997.
38. Karlon WJ, Lehr JL, Eisenberg SR: Finite element models of thoracic conductive anatomy: sensitivity to changes in inhomogeneity and anisotropy. *IEEE Trans Biomed Eng* 41: 1010-1017, 1994.
39. Panescu D, Webster JG, Tompkins WJ, Stratbucker RA: Optimization of cardiac defibrillation by three-dimensional finite element modeling of the human thorax. *IEEE Trans Biomed Eng* 42: 185-192, 1995.
40. Kothiyal KP, Shankar B, Fogelson LJ, Thakor NV: Three-dimensional computer model of electric fields in internal defibrillation. *Proc IEEE* 76: 720-730, 1988.
41. Jorgenson DB, Haynor DR, Bardy GH, Kim Y: Computational studies of transthoracic and transvenous defibrillation in a detailed 3-D human thorax model. *IEEE Trans Biomed Eng* 42: 172-184, 1995.
42. Ng KT, Hutchinson SA, Gao S: Numerical analysis of electrical defibrillation. The parallel approach. *J Electrocardiol* 28 (suppl.): 15-20, 1995.
43. Claydon FJ, III, Pilkington TC, Tang ASL, Morrow MN, Ideker RE: A volume conductor model of the thorax for the study of defibrillation fields. *IEEE Trans Biomed Eng* 35: 981-992, 1988.
44. Oostendorp T, van Oosterom A: The potential distribution generated by surface electrodes in inhomogeneous volume conductors of arbitrary shape. *IEEE Trans Biomed Eng* 38: 409-417, 1991.
45. Gale TJ, Johnston PR, Kilpatrick D, Nickolls PM: Implantable defibrillator electrode comparison using a boundary element model. In: *Proc 16th Ann Int Conf IEEE Eng Med Biol Soc*, IEEE Press, New York, pp. 31-32, 1994.
46. Gale TJ: Modelling the Electric Field from Implantable Defibrillators. PhD thesis, University of Tasmania, Hobart, Tasmania, Australia, 1995.
47. Camacho MA, Lehr JL, Eisenberg SR: A three-dimensional finite element model of human transthoracic defibrillation: paddle placement and size. *IEEE Trans Biomed Eng* 42: 572-578, 1995.
48. Schmidt JA, Johnson CR: DefibSim: an interactive defibrillation device design tool. In: *Proc 17th Ann Intl Conf IEEE Eng Med Biol Soc*, IEEE Press, New York, pp. 305-306, 1995.
49. van Oosterom A, Huiskamp GJM: Implicit and explicit constraints in inverse electrocardiography. *J Electrocardiol* 25 (Suppl.): 87-92, 1992.
50. Gulrajani RM, Savard P, Roberge FA: The inverse problem in electrocardiography: Solutions in terms of equivalent sources. *CRC Crit Rev Biomed Eng* 16: 171-214, 1988.
51. Gulrajani RM, Roberge FA, Savard P: The inverse problem of electrocardiography. In: Macfarlane PW, Lawrie TDV (Eds): *Comprehensive Electrocardiology*. Pergamon Press, Oxford, England, pp. 237-288, 1989.
52. MacLeod RS, Brooks DH: Recent progress in inverse problems in electrocardiology. *IEEE Eng Med Biol Magazine* 17(1): 73-83, 1998.
53. Arthur RM, Geselowitz DB, Briller SA, Trost RF: Quadrupole components of the human surface electrocardiogram. *Am Heart J* 83: 663-677, 1972.
54. Forsythe GE, Moler CB: *Computer Solution of Linear Algebraic Systems*, Prentice Hall, Englewood Cliffs, NJ, p 16, 1967.
55. Ralston A, Rabinowitz P: *A First Course in Numerical Analysis*, McGraw-Hill, New York, chapter 8, 1978.
56. Gulrajani RM, Pham-Huy H, Nadeau RA, Savard P, de Guise J, et al: Application of the single moving dipole inverse solution to the study of the Wolff-Parkinson-White syndrome in man. *J Electrocardiol* 17: 271-288, 1984.
57. Forsythe GE, Malcolm MA, Moler CB: *Computer Methods for Mathematical Computations*. Prentice Hall, Englewood Cliffs, NJ, p 192, 1977.
58. Okamoto Y, Teramachi Y, Musha T: Limitation of the inverse problem in body surface potential mapping. *IEEE Trans Biomed Eng* 30: 749-754, 1983.
59. Tikhonov AN, Arsenin VY: *Solutions of Ill-Posed Problems*, Winston, Washington, DC, 1977.
60. Varah JM: A practical examination of some numerical methods for linear discrete ill-posed problems. *SIAM Review* 21: 100-111, 1979.
61. Soucy B: Etude des problèmes direct et inverse de l'électrocardiographie à l'aide d'un modèle expérimental coeur-torse, MScA thesis, Ecole Polytechnique, Université de Montréal, Montreal, Canada, 1990.
62. Morozov VA: *Methods for Solving Incorrectly Posed Problems*, Springer-Verlag, New York, pp. 44-47, 1984.
63. Groetsch CW: *The Theory of Tikhonov Regularization for Fredholm Equations of the First Kind*, Pitman Publishing, London, pp. 43-52, 1984.
64. Johnson CR: The Generalized Inverse Problem in Electrocardiography: Theoretical, Computational, and Experimental Results. PhD thesis, The University of Utah, Salt Lake City, UT, 1990.
65. Johnson CR: The generalized inverse problem in electrocardiography. In: *Proc 12th Ann Int Conf IEEE Eng Med Biol Soc*, IEEE Press, New York, pp. 593-594, 1990.
66. Wahba G: Practical approximate solutions to linear operator equations when the data are noisy. *SIAM J Num Anal* 14: 651-667, 1977.
67. Golub GH, Heath M, Wahba G: Generalized cross-validation as a method for choosing a good ridge parameter. *Technometrics* 21: 215-223, 1979.
68. Colli Franzone P, Guerri L, Taccardi B, Viganotti C: Finite element approximation of regularized solutions of the inverse potential problem of electrocardiography and applications to experimental data. *Calcolo* 22: 91-186, 1985.
69. Colli Franzone P, Guerri L, Tentonia S, Viganotti C, Baruffi S, et al: A mathematical procedure for solving the inverse potential problem of electrocardiography. Analysis of the time-space accuracy from in vitro experimental data. *Math Biosci* 77: 353-396, 1985.
70. Hansen PC: Truncated singular value decomposition solutions to discrete ill-posed problems with ill-determined numerical rank. *SIAM J Sci Stat Comput* 11: 503-518, 1990.
71. Hansen PC: Analysis of discrete ill-posed problems by means of the L-curve. *SIAM Rev* 34: 561-580, 1992.
72. Miller K: Least squares methods for ill-posed problems with a prescribed bound. *SIAM J Math Anal* 1: 52-74, 1970.
73. Lawson CL, Hanson RJ: *Solving Least Squares Problems*, Prentice Hall, Englewood Cliffs, NJ, 1974.
74. Hansen PC, O'Leary DP: The use of the L-curve in the regularization of discrete ill-posed problems. *SIAM J Sci Stat Comput* 14: 1487-1503, 1993.
75. Johnston PR, Gulrajani RM: A new method for regularization parameter determination in the inverse problem of electrocardiography. *IEEE Trans Biomed Eng* 44: 19-39, 1997.
76. Twomey S: On the numerical solution of Fredholm integral equations of the first kind by the inversion of the linear system produced by quadrature. *JACM* 10: 97-101, 1963.
77. Iakovidis I, Gulrajani RM: Improving Tikhonov regularization with linearly constrained optimization: Application to the inverse epicardial potential solution. *Math Biosci* 112: 55-80, 1992.
78. Oster H, Rudy Y: Regional regularization of the electrocardiographic inverse problem: a model study using spherical geometry. *IEEE Trans Biomed Eng* 44: 188-199, 1997.
79. Pilkington TC, Morrow MN: The usefulness of multipoles in electrocardiography. *CRC Crit Rev Biomed Eng* 7: 175-192, 1982.
80. Beetner DG: Inference of Spectral and Temporal Characteristics of Pericardial Potentials Using Individualized Human Heart-Torso Models and the Multipole-Equivalent Method. DSc dissertation, Washington Univ, St Louis, MO, 1997.
81. Barr RC, Spach MS: Inverse calculation of QRS-T epicardial potentials from body surface potential distributions for normal and ectopic beats in the intact dog. *Circ Res* 42: 661-675, 1978.
82. Throne RD, Olson LG: A generalized eigen-system approach to the inverse problem of electrocardiography. *IEEE Trans Biomed Eng* 41: 592-600, 1994.
83. Throne RD, Olson LG: The effects of errors in assumed conductivities and geometry on numerical solutions to the inverse problem of electrocardiography. *IEEE Trans Biomed Eng* 42: 1192-1200, 1995.
84. Johnston PR: The potential for Laplacian maps to solve the inverse problem of electrocar-

(continued on page 122)

- simulated sulcus of the brain. *IEEE Trans Bio Med Engr*, BME 41:470-479, 1994.
6. Wang JZ: Minimum-norm least-squares estimation: magnetic source images for a spherical model. *IEEE Trans Bio Med Engr*, BME 40:387-396, 1993.
  7. Ary JP, Klein SA, Fender DH: Location of sources of evoked potentials: Corrections for skull and scalp thicknesses. *IEEE Trans Bio Med Engr* BME 28:447-452, 1981.
  8. Stok, CJ: The influence of model parameters on EEG/MEG single dipole source estimates. *IEEE Trans Bio Med Engr* BME 34:289-296, 1987.
  9. Cuffin BN: Effects of head shape on EEG's and MEG's. *IEEE Trans Bio Med Engr*, BME 37:44-52, 1990.
  10. Cuffin BN: Effects of local variations in skull and scalp thickness on EEG's and MEG's. *IEEE Trans Bio Med Engr*, BME 40:42-48, 1993.
  11. He B, Musha T, Okamoto Y, Homma S, Nakajima Y, Sato T: Electric dipole tracing in the brain by means of the boundary element method and its accuracy. *IEEE Trans Bio Med Engr*, BME 34:406-414, 1987.
  12. Kavanagh RN, Darcey TM, Lehmann D, Fender DH: Evaluation of methods for three-dimensional localization of electrical sources in the human brain. *IEEE Trans Bio Med Engr*, BME 25:421-429, 1978.
  13. Cuffin BN, Cohen D, Yunokuchi K, Maniewski R, Purcell C, et al.: Tests of EEG localization accuracy using implanted sources in the human brain. *Ann Neurology*, 29:132-138, 1991.
  14. Cuffin BN: EEG localization accuracy improvements using realistically shaped head models. *IEEE Trans Bio Med Engr*, BME 47:299-303, 1996.

## The Forward and Inverse Problems of Electrocardiography

(continued from page 101)

- diography. *IEEE Trans Biomed Eng* 43: 384-393, 1996.
85. He B, Wu D: A bioelectric inverse imaging technique based on surface Laplacians. *IEEE Trans Biomed Eng* 44: 529-538, 1997.
  86. He B: Theory and applications of body-surface Laplacian ECG mapping, this issue, pp. 102-109
  87. van Oosterom A, Oostendorp TF: On computing pericardial potentials and current densities in inverse electrocardiography. *J Electrocardiol* 25 (Suppl):102-106, 1992.
  88. Horáček BM, Clements JC: The inverse problem of electrocardiography: A solution in terms of single- and double-layer sources on the epicardial surface. *Math Biosciences* 144: 119-154, 1997.
  89. Oster H, Rudy Y: The use of temporal information in the regularization of the inverse problem of electrocardiography. *IEEE Trans Biomed Eng* 39: 65-75, 1992.
  90. Brooks DH, Maratos GM, Ahmad G, MacLeod RS: The augmented inverse problem of electrocardiography: combined time and space regularization. In: *Proc 15th Ann Int Conf IEEE Eng Med Biol Soc*, IEEE Press, New York, pp 773-774, 1993.
  91. Brooks DH, Ahmad G, MacLeod RS: Multiply constrained inverse electrocardiography: combining temporal, multiple spatial, and interactive regularization. In: *Proc 16th Ann Int Conf IEEE Eng Med Biol Soc*, IEEE Press, New York, pp 137-138, 1994.
  92. Greensite F: Second-order approximation of the pseudoinverse for operator deconvolutions and families of ill-posed problems. *SIAM J App Math*, in press, 1998.
  93. Joly D, Goussard Y, Savard P: Time-recursive solution to the inverse problem of electrocardiography: a model-based approach. In: *Proc 15th Ann Int Conf IEEE Eng Med Biol Soc*, IEEE Press, New York, pp. 767-768, 1993.
  94. El-Jakl J, Champagnat F, Goussard Y: Time-space regularization of the inverse problem of electrocardiography. In: *Proc 17th Ann Int Conf IEEE Eng Med Biol Soc*, IEEE Press, New York, pp. 213-214, 1995.
  95. Ahmad GF, Brooks DH, MacLeod RS: An admissible solution approach to inverse electrocardiography. *Ann Biomed Eng*, 26:278-292, 1998.
  96. Oster H, Taccardi B, Lux RL, Ershler PR, Rudy Y: Noninvasive electrocardiographic imaging: reconstruction of epicardial potentials, electrograms, and isochrones and localization of single and multiple electrocardiac events. *Circulation* 96: 1012-1024, 1997.
  97. Johnston PR, Gulrajani RM: Unpublished.
  98. Greensite F, Huiskamp G: An improved method for estimating epicardial potentials from the body surface. *IEEE Trans Biomed Eng* 45: 98-104, 1998.
  99. Cuppen JJM: Calculating the isochrones of ventricular depolarization. *SIAM J Sci Stat Comput* 5: 105-120, 1984.
  100. Cuppen JJM, van Oosterom A: Model studies with the inversely calculated isochrones of ventricular depolarization. *IEEE Trans Biomed Eng* 31: 652-659, 1984.
  101. Colli Franzone P, Guerri L, Viganotti C: Oblique dipole layer potentials applied to electrocardiology. *J Math Biol* 17: 93-124, 1983.
  102. Huiskamp G, van Oosterom A: The depolarization sequence of the human heart surface computed from measured body surface potentials. *IEEE Trans Biomed Eng*. 35: 1047-1058, 1988.
  103. Huiskamp G, van Oosterom A: Tailored versus realistic geometry in the inverse problem of electrocardiography. *IEEE Trans Biomed Eng* 36: 827-835, 1989.
  104. Huiskamp G, van Oosterom A: Heart position and orientation in forward and inverse electrocardiology. *Med & Biol Eng & Comput* 30: 613-620, 1992.
  105. Greensite F: Topological foundations of electrocardiology. *Advances App Math* 6: 230-258, 1985.
  106. Greensite F: Some imaging parameters of the oblique dipole layer cardiac generator derivable from body surface electrical potentials. *IEEE Trans Biomed Eng* 39: 159-164, 1992.
  107. Greensite F: Remote reconstruction of confined wavefront propagation. *Inv Prob* 11: 361-370, 1995.
  108. Huiskamp G, Greensite F: A new method for myocardial activation imaging. *IEEE Trans Biomed Eng* 44: 433-446, 1997.
  109. Schmidt R: Multiple emitter location and signal parameter estimation. *IEEE Trans Antennas Propagat* 34: 276-280, 1984.